The thesis committee for Ekrem Alagoz certifies that this is the approved version of the following thesis:

Interaction of Fracturing Fluids with Shales: Proppant Embedment Mechanisms

APPROVED BY

SUPERVISING COMMITTEE

Mukul Sharma, Supervisor

D. Nicolas Espinoza

Interaction of Fracturing Fluids with Shales: Proppant Embedment Mechanisms

by

Ekrem Alagoz

Thesis

Presented to the Faculty of the Graduate School

of the University of Texas at Austin

in Partial Fulfillment

of the Requirements

for the degree of

Master of Science in Engineering

The University of Texas at Austin

December 2020

Dedication

To my country.

Acknowledgments

Firstly, I am grateful to The Almighty Allah for allowing me to complete this master's degree.

I would like to extend my sincerest gratitude to my advisor Dr. Mukul M. Sharma, for giving me the opportunity to contribute to his research program and also for his support, guidance, constructive criticism, and patience throughout my research at The University of Texas at Austin. His guidance helped me throughout my research and in writing this thesis. I could not have imagined having a better advisor and mentor for my graduate study.

Besides my supervisor, I would like to thank Dr. Nicolas Espinoza for being the second reader for my thesis. I am also appreciative of Dr. Haotian Wang for answering my theoretical questions. A special thanks to Rodney T. Russell, our lab manager, for developing experimental setups for my tests and his invaluable suggestions about my experiments, Jin Lee, for her administrative support.

I would like to thank all my department colleagues and friends for their help, support, and friendship. I also thank my lab mates in our group; Zach Quintanilla, Williams Osagie Ozowe, Noor Kouli, and Fatimah AlNasser; Graduate Program Coordinator Amy D. Stewart and Academic Program Coordinator Jessica M. Yeager.

I would also like to thank The Republic of Turkey and the General Directorate of Mineral Research and Exploration (MTA) for their financial support. Finally, I would like to thank my parents and all my family for their endless, unique support and unconditional love.

Abstract

Interaction of Fracturing Fluids with Shales: Proppant Embedment Mechanisms

Ekrem Alagoz, M.S.E.

The University of Texas at Austin, 2020

Supervisor: Mukul Sharma

In petroleum engineering, hydraulic fracturing has been developed to mitigate the crucial problem of the world's dwindling oil supplies. Thanks to hydraulic fracturing, engineers can create new artificial apertures with pressurized fluids. The process includes the high-pressure injection of a fracking fluid, which is basically water and proppants. Hydrocarbons will flow more freely after the flow back of water. Once the pumping of fracturing fluid is stopped, created fractures begin to close, as the stress increases. This has become a critical issue because closing these fractures results in a rapid decline in productivity of the well. The primary reason for proppant usage is to settle between fracture apertures and prop them open in order to increase oil and gas productivity.

Proppant embedment is a crucial problem that causes many fractures to fail over time. Fractured well productivity can be dramatically reduced by severe proppant embedment due to a reduction in fracture aperture. Accordingly, understanding the proppant embedment phenomena is essential for hydraulic fracturing treatments. In this thesis, the mechanisms of proppant

embedment have been investigated by quantifying the stress-dependent deformations (elastic and plastic) as well as the time-dependent deformation (creep).

A set of constitutive equations were developed to account for elastic, plastic, and creep deformation during proppant embedment. Two new experimental apparatuses have been built and used to quantify the shale rock proppant deformation behavior (elastic, plastic, and creep) after exposure to various fracture fluid additives such as surfactants and clay stabilizers. Results show that proppant embedment primarily occurs due to plastic deformation followed by time-dependent creep deformation, while elastic deformation is small. The impact of different fracturing fluids and rock mineralogy on proppant embedment were also studied. Our results show that fluid chemistry substantially affects the amount of plastic deformation and creep. For example, KCI with a Clay Inhibitor was quite successful in reducing the proppant embedment. Shales with high clay-content embedded proppant at lower stresses and showed more plastic deformation. The test results show that 15% more clay-content shale samples experienced almost 50% more deformation. Chemical treatments fostered the best improvements or degradations in high clay-content shales.

Table of Contents

List of Figures

List of Tables

Chapter 1: Introduction

1.1 Importance of Proppant Embedment

In the light of the world's dwindling oil reserves, new methods have been developed to increase oil and gas extraction from vast shale deposits. Among the many proposed solutions, hydraulic fracturing, commonly referred to as fracking, has garnered much attention over the last decades in the United States.

The technique of hydraulic fracturing involves injecting fluid with proppant into a formation at very high pressures, which bring about fracking the rock in very complex geometry. Proppants are hard particulate materials, most commonly sand, that are mixed with the fracturing fluid and pumped into the fractures as they form. When the proppant is successfully settled between the fracture apertures, the proppant holds the fracture open after the fracturing fluid pressure drops. Proppants settle between the fracture surfaces to keep fractures open for hydrocarbon flow. Proppants play an essential role in the hydraulic fracturing treatment because they maintain a conductive flow path in shale formations since reservoir fluids will flow more freely with proppant in the fractures. Proppants are pumped with fracking fluid, which suspends the proppant to avoid settling in the beginning and transport these sands through the fracture apertures.

Fracture apertures start to close after the flow back of the fracturing fluid. Fracture closure is affected by several different phenomena, including proppant embedment, fines generation and migration, proppant crush resistance, reorientation of proppants, and proppant flow back (Sato and Ichikawa, 1998; Economides and Nolte, 1989; Reinicke et al., 2006, 2010; Alramahi and Sundberg, 2012; Terracina et al., 2010), fracture closure stress, proppant concentration, and

distribution, formation hardness, surface roughness (Volk et al., 1981), water saturation, dynamic fluid leak-off, cyclic loading conditions (Lacy et al., 1998) fracturing fluid viscosity (Lacy et al., 1997; Corapcioglu et al., 2014), shale rock mineralogy (Alramahi and Sundberg, 2012), elastic, creep deformation (Guo and Liu, 2012), and pumping strategy (Huang et al., 2019). These factors are presented in Figure 1.

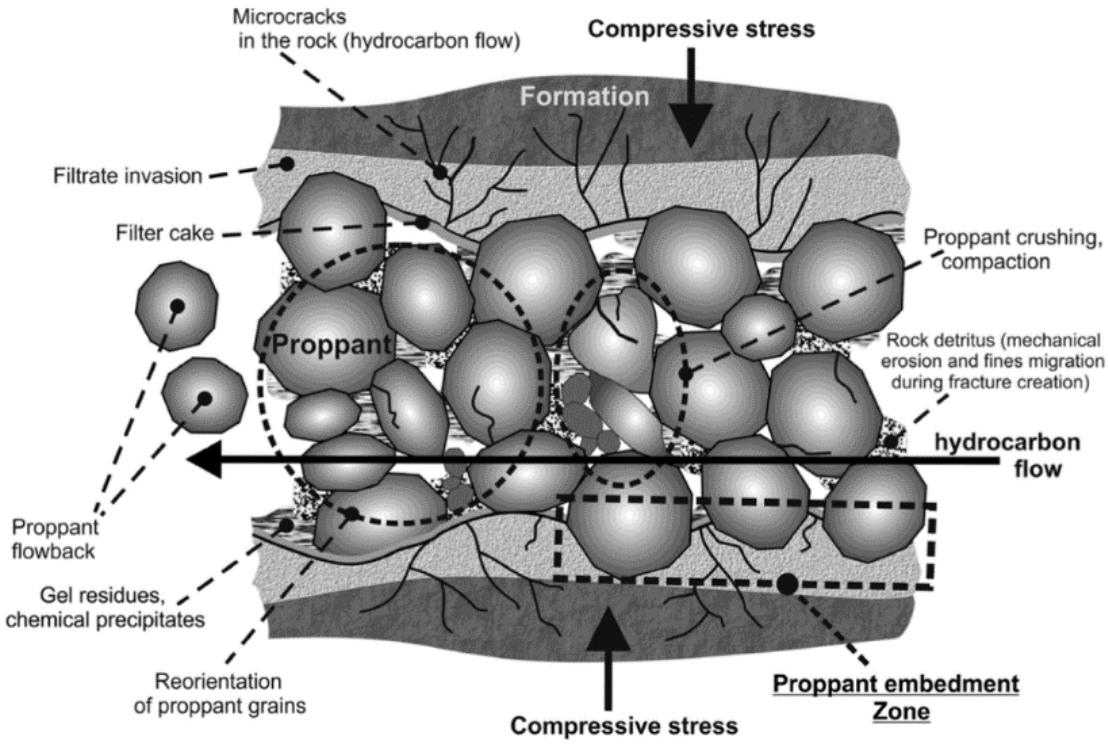

Figure 1. Schematic Figure of Proppant Placement. (From Maslowski et al., 2018)

It is essential to understanding proppant embedment mechanisms to maximize fracture flow capacity and enhance hydrocarbon recovery. Proppant embedment can reduce fracture gap by almost 75% in poorly consolidated sandstone reservoirs. Additionally, even a 20% reduction in the fracture gap would reduce hydrocarbon production by over 50% (Lacy et al., 1998). A better understanding and systematic study of embedment mechanisms in shale rock formations are required. Fracture closure is a complex problem governed by many variables. This thesis examines

proppant embedment phenomena studied on unconventional shale rocks by measuring the elastic, plastic, and creep deformation of the rock under stress. Factors other than proppant embedment are beyond the scope of this thesis.

1.2 Thesis Outline

This thesis is partitioned into six chapters. Chapter 2 gives a general overview of proppants, including their definition, advantages, historical use, and recent applications. Chapter 3 presents two new experimental setups to account for rock deformation behaviors and test results. The scope of the study is introduced in Chapter 4, including the development of the elasto-viscoplastic model, used for data analysis in this thesis and calculation of elastic, plastic, and creep deformations. In Chapter 5, proppant embedment test results are given. Finally, Chapter 6 presents the conclusions and recommendations for future works. PYTHON codes, and derivation of equations can be found in the Appendices of this thesis.

Chapter 2: Literature Review

2.1 Overview

This chapter discusses the role of proppants and their usage in hydraulic fracturing operations. It discusses the present-day proppant products, fluid and proppant selection, proppant transport, proppant embedment, and elements that affect fracture conductivity.

2.2 Introduction

In the past, hydrocarbon production from shale rock formations was believed to be uneconomical since shales have tiny pore sizes, nano-Darcy range permeability, and very complex mechanical rock properties. Also, changes and subtle differences in mineral content cause laminations, which lead to anisotropy in numerous rock properties, including electrical resistivity, permeability, Poisson's ratio, moduli, and acoustic velocity (Waters et al. 2011). These characteristics of shale rock formations make hydrocarbon production very challenging, and production is only economically feasible because of hydraulic fracturing. The advancements in hydraulic fracturing and horizontal drilling technology made shale formations practical to produce.

Hydraulic fracturing has improved significantly over the last decades. The hydraulic fracturing treatment is initiated by injecting a large amount of water or polymer solution with granular solid material (proppant) at a very high flow rate, thereby exceeding the formation breakdown pressure to create conductive pathways (fractures) for enhancing the productivity of hydrocarbon resources. Proppants are fundamental elements of hydraulic fracturing. The generated fractures will close shortly without proppant; this will significantly limit the desired well performance (Howard and Fast 1970). The following sections discuss more proppant specifications.

2.3 Proppant Types and Proppant Selection Criteria

2.3.1 Proppant Types

Since shale reservoirs have minimal permeability, it is crucial to optimize the fracturing fluid and proppant specifications to obtain the best fracture behavior with the least mechanical and chemical damage to the shale. There are three major types of proppant used in the oil and gas industry. These are natural sands, ceramic proppants, and resin-coated proppants. Figure 2 shows the breakdown of volume usage of these proppant types. As can be seen in Figure 2, natural sands are the most widely used proppant type.

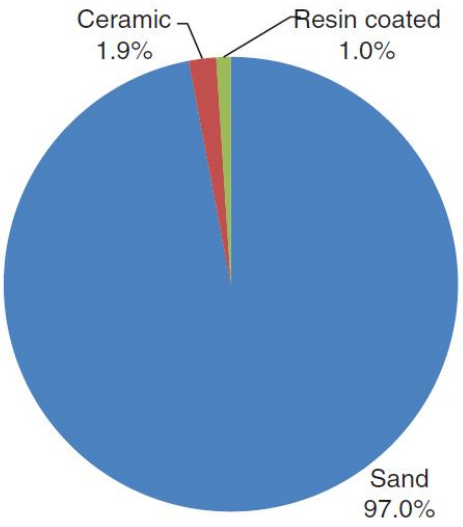

Figure 2. Global Proppant Consumption by Proppant Type. (From PropTester Inc. and Kelrik LLC, 2019)

While natural sands dominate the proppant market, ceramic and resin-coated type proppants are still used in many cases. Figure 3 illustrates the total global consumption of proppants for these three types.

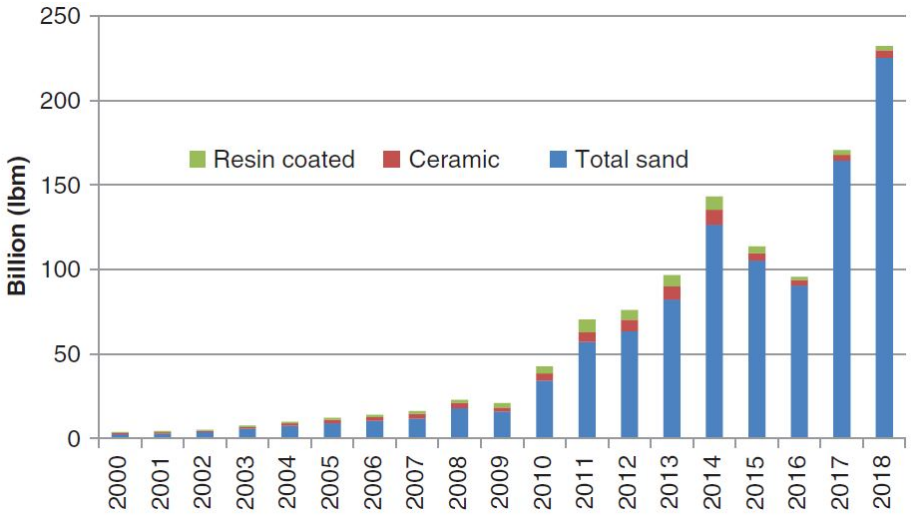

Figure 3. Total Global Proppant Consumption. (From PropTester Inc. and Kelrik LLC, 2019)

Unlike natural sands, ceramic proppants are artificially manufactured materials. Ceramic proppants were first introduced in the industry in the 1970s. Since ceramics have a micro-crystalline structure, they are higher-strength proppants and shows better performance when experiencing high closure stresses. There are three types of ceramic proppants, including High-Density Ceramics (HDC), Intermediate Density Ceramics (IDC), and Lightweight or Low-Density Ceramics (LWC/LDC). Figure 4, Figure 5, and Figure 6 show these proppants.

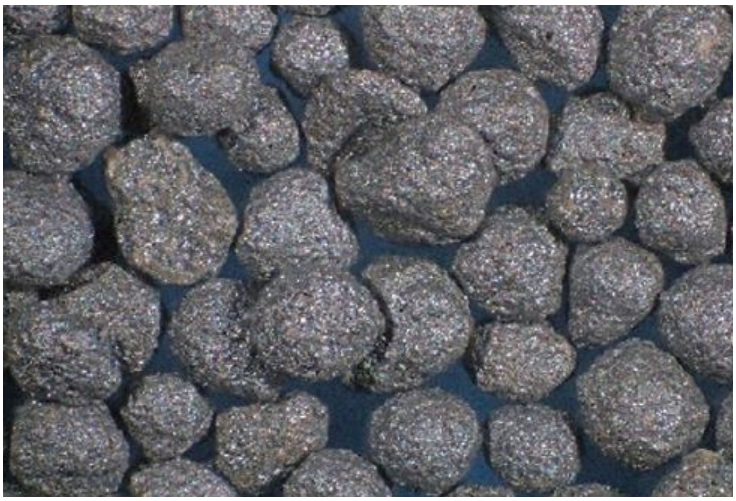

Figure 4. High Strength Ceramic Proppants. (From Miskimins, 2019)

Figure 5. Intermediate Strength Ceramic Proppants. (From Miskimins, 2019)

Figure 6. Low Strength Ceramic Proppants. (From Miskimins, 2019)

Alumina content and density make the differences among these proppant types. The higher the alumina content, the higher the density, and the higher the strength. For example, intermediate-density ceramics contains 70 to 75% in aluminum oxide (Fitzgibbon 1984), and more information is tabulated in Table 1. The rest is comprised of silicon dioxide and earth oxides (less than 5%) (Palisca and Saldungaray, 2013).

Table 1. Ceramic Proppant Specifications

Ceramic Types	Alumina Content (%)	Density (g/cc)	Strength Range
HDC	80-85	3.6	High
IDC	70-75	3.3	Intermediate
LDC/LWC	45-50	2.27	Low

Proppant pack cyclic stress resistance is an essential factor to consider in fracturing proppant selection. During the production, various events lead to cyclic stress changes. These stress changes often caused uncoated proppants, especially brittle ceramics, to fail prematurely under challenging downhole conditions. Resin-coated proppants distribute these stress changes thanks to an elastic bond they create and the load on each proppant grain is reduced. This feature leads to reduce fines generation and improve proppant pack integrity (Greff et al. 2014; Graham et al. 1975; Johnson and Armbruster 1982).

2.3.2 Proppant Selection Criteria

Choosing the right proppant is not a simple question to answer owing to the uncertainties in the rock itself and fracture complexity. In conventional wells, the average proppant cost varies from 10 to 40% of the drilling and well completion cost, contingent upon the proppant type and fracturing treatment operation (Wilcox et al. 2015). Proppant optimization may be the determining factor for the success of the fracturing operation, which makes the proper proppant selection even more critical. Several concerns inform proppant selection, such as the severity of fines generation, the amount of embedment, and the degree of fracture closure stresses.

Proppant fines are the small broken parts of the proppant generated by crushing. These fines block the pathways, thus the fracture conductivity. Coulter et al. (1972) show that only 5%

of fines cause a deduction in proppant pack conductivity by 50%. Lacy et al. (1997) conclude that 5% of fines generation causes an almost 60% reduction in conductivity. Blauch et al. (1999) and Weaver et al. (1999) report that formation fines can limit the conductivity over 90%.

Additionally, proppant embedment plays an essential role in the reduction of fracture width, which limits hydrocarbon flow. Lacy et al. (1998) stated that proppant embedment can reduce the fracture gap in the range of 10 to 60%. A 15% reduction in the opening of fracture can reduce fluid flow up to 60%. Fracture closure stresses is another critical parameter to obtain optimum proppant pack stabilization. Andrews et al. (1998) show that the increase in closing stress may increase the drag forces among the independent grains, which leads to a more stable proppant pack. On the other hand, excessive stress can initiate the reflux of the proppants and lead to some grain breakage. Milton-Tyler et al. (1992) did an experimental study, and results show that the severity of proppant embedment has a significant effect on proppant pack stabilization. Consequently, all these parameters should be kept in mind when choosing proppants.

2.4 Fracturing Fluids and Its Additives

Due to the intricate rock properties of shale reservoirs such as permeability, mineral structure, total hydrocarbon content, it is necessary to optimize the fracturing fluids used in hydraulic fracturing operations. Anderson et al. (1982) have outlined the problems, including metal corrosion, gel-residue, fluid compatibility, matrix compatibility, fluid leak-off, and fluid flow back, which fracturing fluids can cause. Therefore, the design of the fracturing fluid becomes a vital factor in fracturing treatments. There are numerous hydraulic fracturing fluid types available such as water-based fluids, oil-based fluids, foam fluids, and energized frac fluids. Figure 7 shows the most common chemicals used in hydraulic fracturing operations in the US.

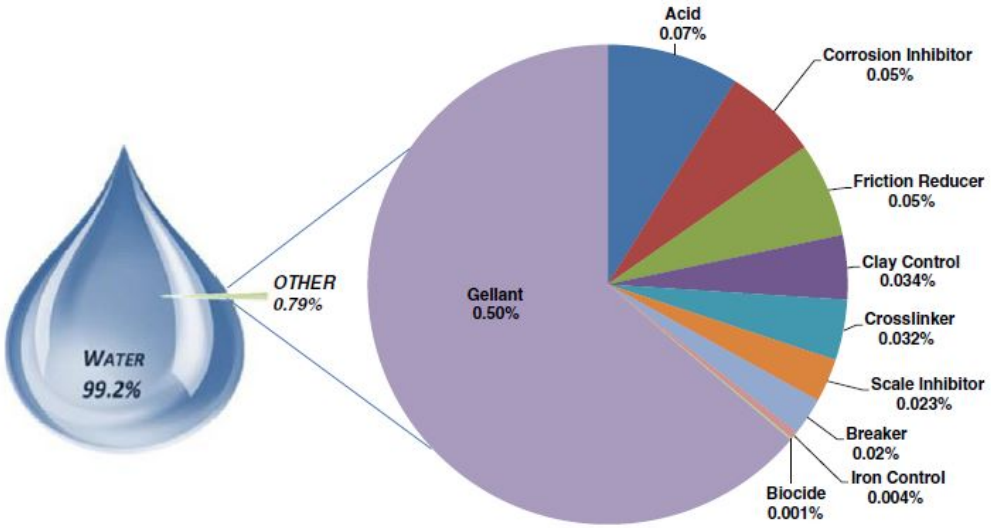

Figure 7. Average Hydraulic Fracturing Fluid Usage for US Shale. (Graph Courtesy of FracFocus.org Data August 2012)

Fracturing fluids are mixed with water and proppants and pumped into the well during the operation. The success of the fracturing treatment depends on the properties of fracturing fluid. We can list the desired fracturing fluid properties as follows: Compatibility with formation and fluids, ability to suspend and transport proppants, easily removed from formations, have low frictional pressure, easy to use and operate in the field, cost-effective, and maintaining its viscosity throughout the hydraulic fracturing operation (Miskimins 2019).

The problems that may arise from fracturing fluid chemicals have been identified and published by many researchers. Some of them can be mentioned as follows; In cases where the fracturing fluid additives cause the clays to swell and trigger fines migration, the fracking operation will fail (Smith et al. 1964; Reed 1972; Monaghan 1959; Jones 1964; Hewitt 1963; Hower 1974; Mungan 1965; Peters and Stout 1977; Bates et al. 1946; Coulter et al. 1983). In some formations, clay control is of great importance, especially since the shale permeability is in the nano-Darcy scale. Besides, the fracturing fluid should not create emulsions or deposits to prevent formation clogging and plugging (Hawsey et al. 1964; Tannich 1975; Clark et al. 1982; Allen and Roberts

1978; API RP 42 1977; Graham et al. 1959; Penny et al. 1983). Further, fracturing fluid or its additives can also dissolve the cementing material, which will lead to spalling problems. Studies show that the importance of paraffin problems caused by fracturing fluids (Featherston et al. 1959; Knox et al. 1962; Sloat 1963; Bauer and Bezemer 1967; Tinsley 1967; McCall and Johnson 1984; Stiff and Davis 1952). Others refer to the characteristic properties the fracturing fluid should have to transport proppants (Daneshy 1978; Novotny 1977; Clark et al. 1977; Hannah and Harrington 1981; Shah 1982; Ford 1960; Clark and Guler 1983; Harris et al. 2009; Shah et al. 2001; Harris 1996; Brannon and Ault 1991; Gdanski et al. 1991).

Most of the fracturing fluid that is pumped into the formation must remain in the fracture. An ideal fluid combines both high viscosity with a low fluid loss, which determines the fluid efficiency (Stewart and Coulter 1959; Hall and Dollarhide 1964, 1968; Hawsey and Jacocks 1961; Gatlin and Nemir 1961; Pye and Smith 1973; King 1977; Shumaker et al. 1978; Settari 1985; Harris 1985, 1987; McDaniel et al. 1985; Zigrye et al. 1985). A highly efficient fracturing fluid forms the desired fracture volume and transports proppants suitably. Finally, fracturing fluids should be low cost, which is one of the most crucial selection parameters. Although the efficiency of the fluid is high, if it is not cost-efficient in terms of economic aspects, then this fluid cannot be used (Powell 1999; Cawiezel et al. 2007; Lawrence et al. 2009; Nolte and Plahn 1993; Samuel et al. 1999; McGowen et al. 1993; Brannon and Ault 1991; Leopoldo 2010; Palmer et al. 1991; Funkhouser et al. 2010; Wheaton et al. 1991; Li et al. 2009; Mirakyan et al. 2009; Gupta 2009; Jennings 1996).

Water-based fluids are commonly used in hydraulic fracturing treatments. While water-based fracturing fluids can be as simple as slickwater, they can also be as complicated as crosslinked polymer fluids with a variety of chemical additives. Water is relatively economical

and readily available in most areas of the world. Also, water-based fluids are incombustible, so they are not a fire hazard, and it can be easily viscosified and adjusted as desired. These advantages make water-based fluids handier, and they are chosen for hydraulic fracturing in most of the reservoirs.

The usage of slick water has also increased, with the improvements in unconventional reservoir managements. Slick water is widely used in low permeability reservoirs since it is economical and plentiful in the fields (Wang and Miskimins, 2010). Slick water contains a friction reducer to minimize the horsepower needed for pumping the fluid down into the well. Furthermore, long, complex fractures can be obtained with the use of slick water (Mayerhofer et al., 2008). Hence, some slick water with a different combination of friction reducers was used in this research.

2.5 Fracturing Conductivity

Operators, service companies, and proppant manufacturers have tried to relate proppant performance with the well productivity index. One of the meaningful ways to do this is to associate the fracture conductivity with the proppant properties. The fracture conductivity is a measure of the rock's capacity to convey the produced fluid. Argawal et al. (1979) described the fracture conductivity, F_{CD}

$$F_{CD} = \frac{k_f \cdot w}{k \cdot x_f} \tag{2.1}$$

where k_f is the fracture permeability, w is the propped fracture width, k is the reservoir permeability, and x_f is the hydraulic half-length (on each side of the well). Fracture conductivity is a function of several parameters, including closure stress, proppant size, proppant distribution, and proppant embedment.

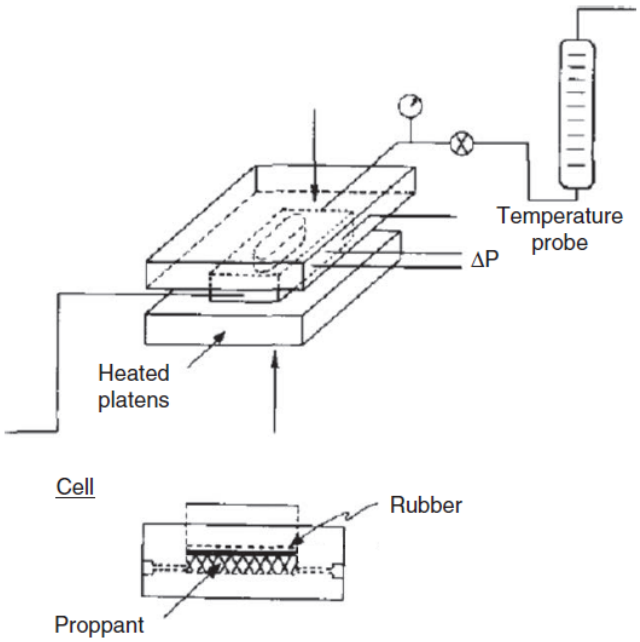

Figure 8. Conductivity Cell. (From Cooke, 1973)

The conductivity of a proppant pack is measured using a standardized conductivity test, which was described by Cooke (1973) in Figure 8. With several years of developments in this study, API RP 61 (1989), *Recommended Practices for Evaluating Short Term Conductivity*, was issued by American Petroleum Institute as the first industry standard for measuring the proppant conductivity. The fracture conductivity unit is shown in Figure 9. During this test, stress is applied by placing the proppants between two metal plates. A fluid is flown between these plates, and the conductivity of the proppants is measured (Cooke 1973; Barree et al. 2003).

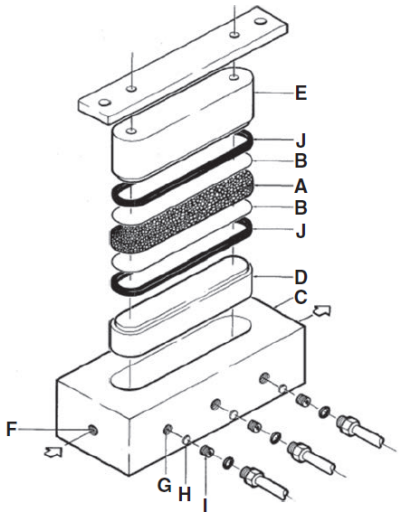

Figure 9. API Short Term Fracture Conductivity Unit. (From API RP61, 1989)

The apparatus called for in *API RP 61* included the following:

A. Proppant pack (6 in. × 1.5 in. × *w*)

B. Metal platen

C. Test unit body

D. Lower piston

E. Upper piston

F. Test-fluid entry/exit port

G. Differential-pressure sensing port

H. Porous metal filter

I. Set screw

The effect of proppant embedment and time-dependent deformation (creep) was not measured in this unit. Changes were proposed in the API test, which lead to a better assessment of

proppant conductivity under reservoir conditions (Much and Penny, 1987), which generally referred to long-term conductivity tests. The modification included replacing metal pistons with sandstone rock samples (Liang et al., 2015; Much and Penny, 1987). Figure 10 shows the effect of the conductivity of steel vs. sandstone. The difference is due to proppant embedment.

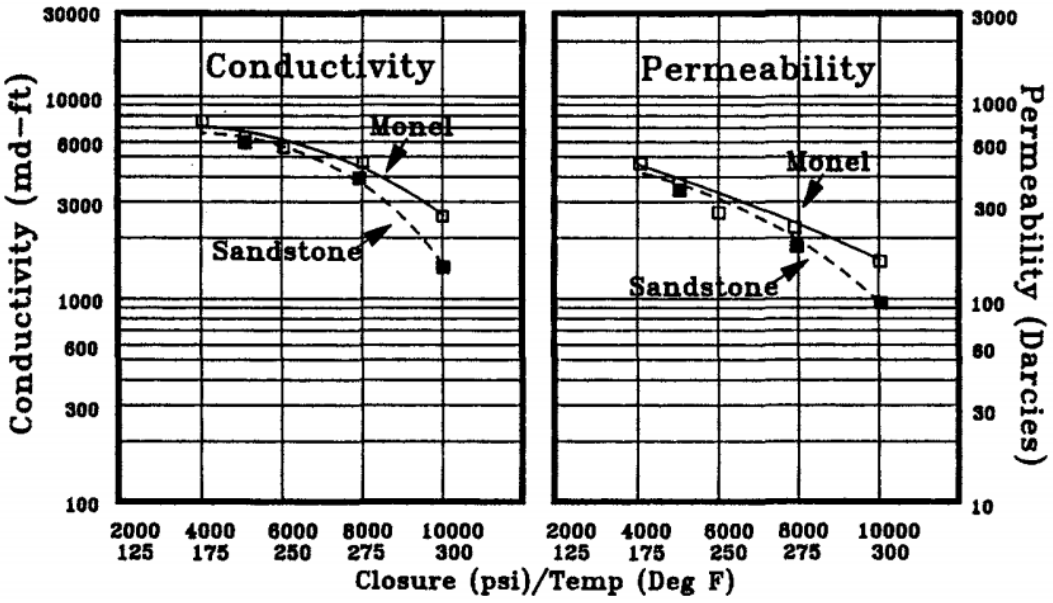

Figure 10. Comparison Long Term Conductivity and Permeabilities Between 2 lb/sq ft 20/40 Interprop Plus Monel Shims(steel) and Ohio Sandstone vs. Closure Stress/Temperature. (From Penny, 1987)

2.6 Proppant Embedment: Previous Work

The components of proppant embedment have been investigated by many researchers from various points of view. Maslowski et al. (2018) state that the proppant embedment phenomenon can be determined by developed testing methodology and reports that determining the fracture surface's deformation represents the proppant embedment phenomenon. They developed a series of experimental testing methods to determine the deformation on shale rocks. Initially, shale rocks were soaked by fracturing fluid before the embedment test at 70°C and 1000 psi for 2 hours. Proppants set between two cylindrical rock cores were used and then compressive stress was

applied. As the next step of this experiment, microscope cameras were used to determine the average depth of proppant embedment. The X-ray diffraction method (XRD) was used to determine the mineral composition in this experiment. They concluded that a method to determine proppant embedment by measuring the deformation would be crucial for assessments of not only proppant type but fracturing fluid selection and optimization.

Alramahi and Sundberg (2012) also did experimental research on proppant embedment. They submerged the shale samples in a brine solution of 3% KCI (by weight) for 24 hours before the embedment test and measured the deformation of shale samples due to proppant embedment by applying axial load. They found that there was a strong correlation between clay content and proppant embedment, as shown in Figure 11. They also used an expression derived by Walsh (1981) to validate their results (Appendix E, Equation F.9).

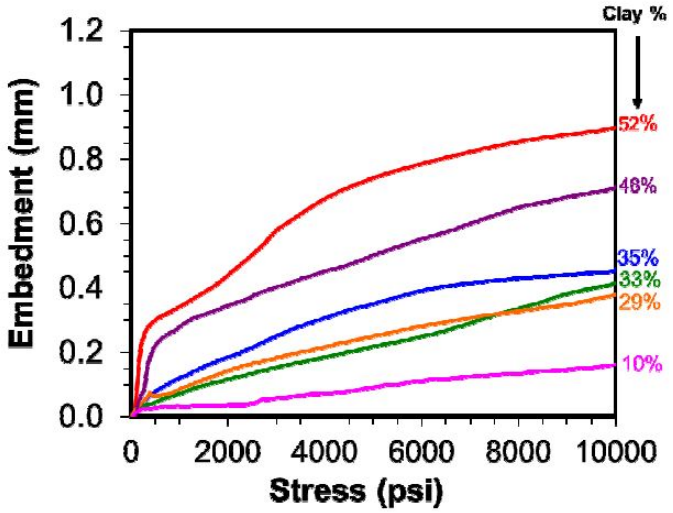

Figure 11. Embedment vs. closure stress (From Alramahi and Sundberg 2012)

Additionally, Corapcioglu et al. (2014) included a temperature effect on proppant embedment. They found that decreasing Young's Modulus or temperature would weaken the

formation, which results in more embedment (Figure 12). When they used deionized water with KCl, they obtained the minimum reduction in Young's Modulus (Figure 13). Adding a friction reducer to this solution caused more reduction in Young's Modulus as well as more proppant embedment.

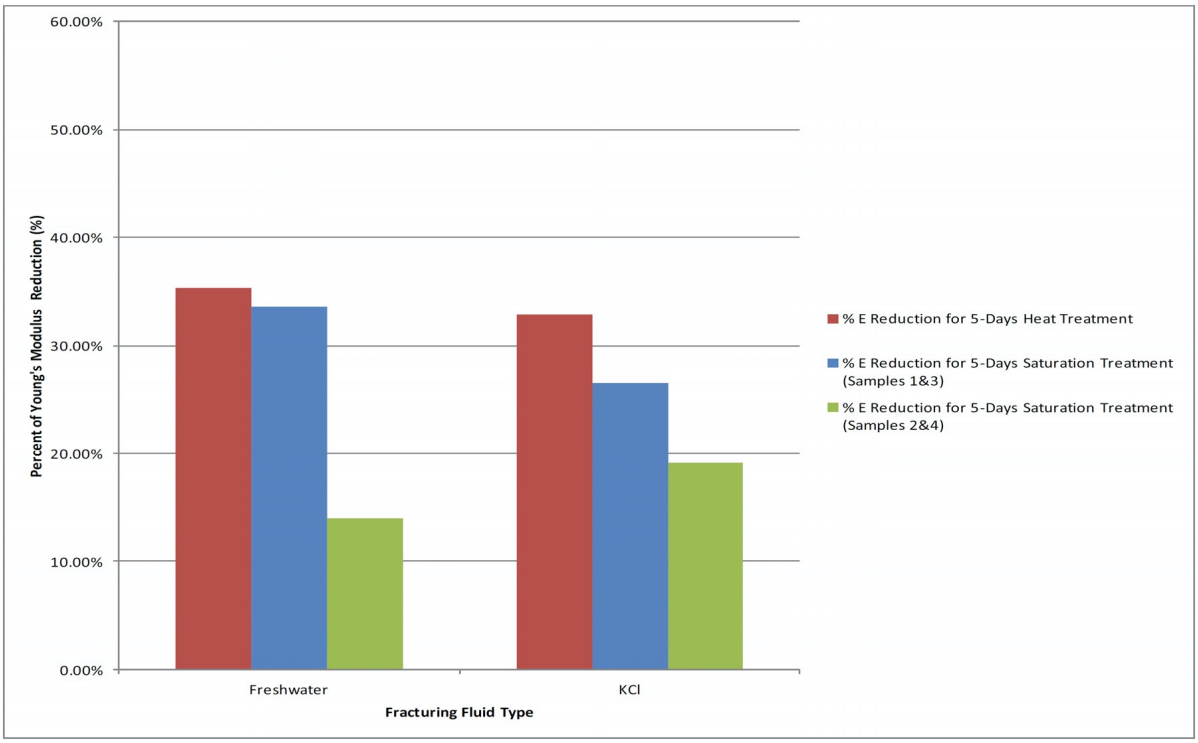

Figure 12. Young's Modulus Reduction Percentage vs. Fracturing Fluid Type. (From Corapcioglu et al. 2014)

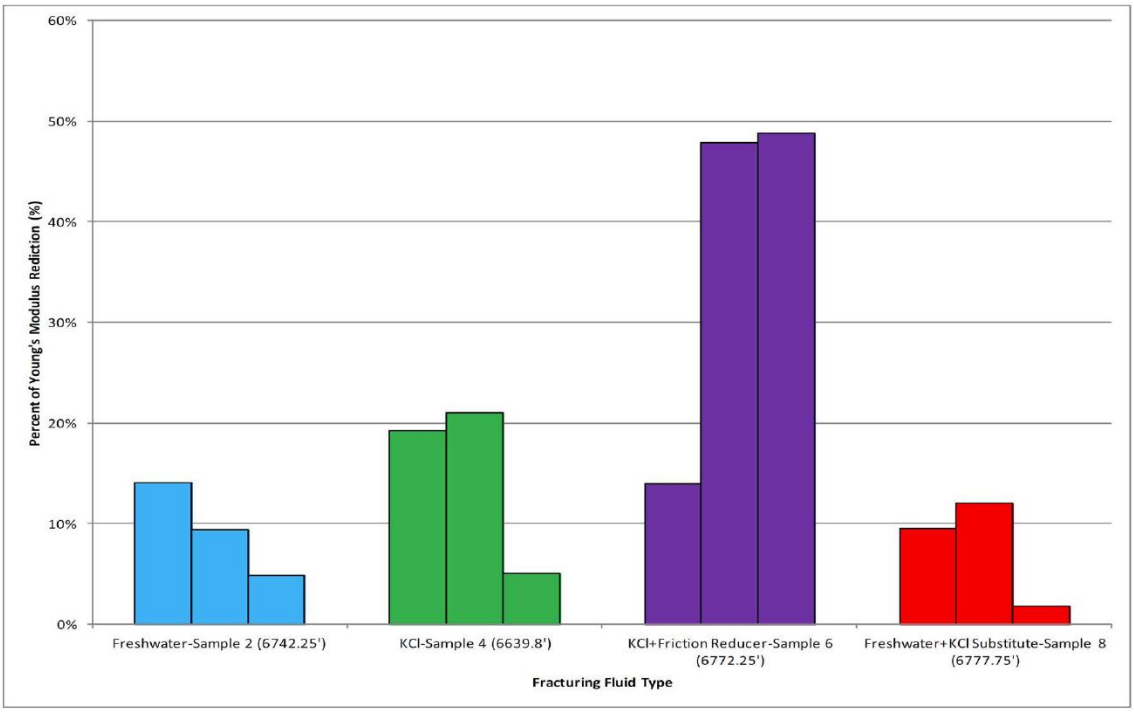

Figure 13. Young's Modulus Reduction Percentage vs. shale samples soaked with different fluids. (From Corapcioglu et al. 2014)

Gao et al. (2013) conducted embedment tests and developed a mathematical method to estimate proppant embedment and conductivity. They reported that conductivity of proppant pack increases with the proppant size, scales with the initial fracture opening, and decreases with increasing closure stress. Huang et al. (2019) developed a model to predict dynamic fracture pressure efficiently and reliably. Their model considered proppant concentration, proppant distribution, and stress condition as well as the formation type. Guo et al. (2012) showed that the Poisson's Ratio has a minimum effect on the proppant embedment by including the elastic and presentation deformations of shale rocks into the calculations.

On the modelling side, a considerable number of mathematical models exist (Cooke, 1973; Huang et al., 2019; Vlis et al., 1975; Guo et al., 2012; Roodhart et al., 1986; Milton-Taylor et al., 1992;). Many of these models, both empirical and semi-empirical, are limited by not considering all the comprehensive aspects present during proppant embedment. Additionally, Guo et al. (2012)

used a viscoelastic model for prediction of embedment and fracture aperture, but they did not study the plastic behavior of rocks.

Although a considerable amount of research has been conducted on the proppant embedment phenomenon experimentally (Corapcioglu et al., 2014; Alramahi and Sundberg, 2012; Maslowski et al., 2018; Terracina et al., 2010), none of them consider all rock deformation behaviors in one experimental setup. For example, Alramahi et al. (2012) did not study fines migration and shale creep. Also, by focusing on cylindrical rock cores, Maslovski et al. (2018) overlooked the effect of mineralogy on embedment.

The sedimentary heterogeneity of shales causes non-uniform mineralogy distribution along shale cross-sections. Shale formation heterogeneity is a dominant difference compared to conventional formations; shale formations are found to be anisotropic due to laminations, which create a difference in properties in directions perpendicular to the bedding planes (Waters et al. 2011). In Maslovski's experiment, every proppant is subject to different stresses depending on the clay content that it sees due to its position. This results in deformation, which varies substantially with the position. Maslovski did not study the effect of mineralogy in his experiments, and this raises a question about his findings.

Chapter 3: Research Method, Experimental Apparatus, and Procedures[1]

3.1 Methodology

This project is an integration of a mathematical model with lab-based experimental studies, which aims to investigate proppant embedment mechanisms. First, a mathematical model was built to account for rock deformation behavior, which includes elastic, plastic, and creep deformation. Two new independent experimental setups were developed to quantify these deformations: a constant load-controlled test and a displacement-controlled test. In the load-controlled test, the shale embedment data includes elastic, plastic, and creep deformation modes. Whereas in the displacement-controlled test (which is a relatively quick test), creep deformation is a minor factor. Stress dependent elastic and plastic deformations can be calculated from displacement-controlled test results, while the load-controlled test provides total deformation of the sample. By using both test results, all three deformations can be obtained individually.

It is crucial to keep an eye on other factors that may affect the embedment test results. Firstly, the proppant crushing problem was eliminated by using a 1 mm diameter tungsten carbide ball bearing, which has very high compressive strength as proppant. Secondly, as the mineralogy may have a considerable effect on shale deformation, the sample compositions were analyzed using x-ray fluorescence (XRF). Since the samples with higher clay content experience more deformation, they were grouped according to mineralogy, then exposed to different fracturing

[1] The content of this chapter was published as: Alagoz, E., Wang, H., Russell, R. T., & Sharma, M. M. (2020, September 18). New Experimental Methods to Study Proppant Embedment in Shales. American Rock Mechanics Association.

fluids to investigate the fluid effect on the rock's mechanical properties. Ideally, these findings could help to optimize fracturing fluids selection.

Furthermore, it is crucial to test the fluid penetration distance of the samples that are being used. Nuclear Magnetic Resonance (NMR) was used to determine liquid volumes in the samples. For example, shale samples were soaked in various fracking fluids for 15 days at atmospheric pressure. The soaking time was picked based on typical shale contact times in the field and further refined as test data developed. Finally, since water-based fluids typically soften shale, NMR tests tracked the amount of shale imbibition seen with different fracturing fluids and shales. Preserved Utica shale samples were used in the embedment tests, while both Utica and Eagle Ford shale samples were used in Nuclear Magnetic Resonance (NMR) and XRF tests. All the Utica shale samples used in this project were from the same preserved core.

3.2 Description of Equipment

3.2.1 Load Controlled Test

A constant load experimental apparatus was designed for the load-controlled tests. In these load-controlled tests, all three–elastic, plastic, and creep–deformations of the shale are measured. Figure 14 shows a schematic of the load-controlled test; the test's main element is a simple Class 2 lever that pushes the proppant into the shale with weights and leverage. This lever configuration also has a geometric advantage that allows for precision measurement since the lever arm's far point moves ten times the distance as the proppant load. The constant load is easily controlled by positioning weights on the lever arm. This load is measured with a load cell placed under the shale sample holder. Figure 15 shows a photo of the actual load-controlled apparatus. In order to minimize error from the apparatus itself, all of the load elements, including the base of the sample holder, have much higher yield strengths and moduli than the shale being measured. Moreover,

the apparatus response was calibrated using a range of material standards ranging from research grade ultra-high-density silicon carbide to low strength polyethylene.

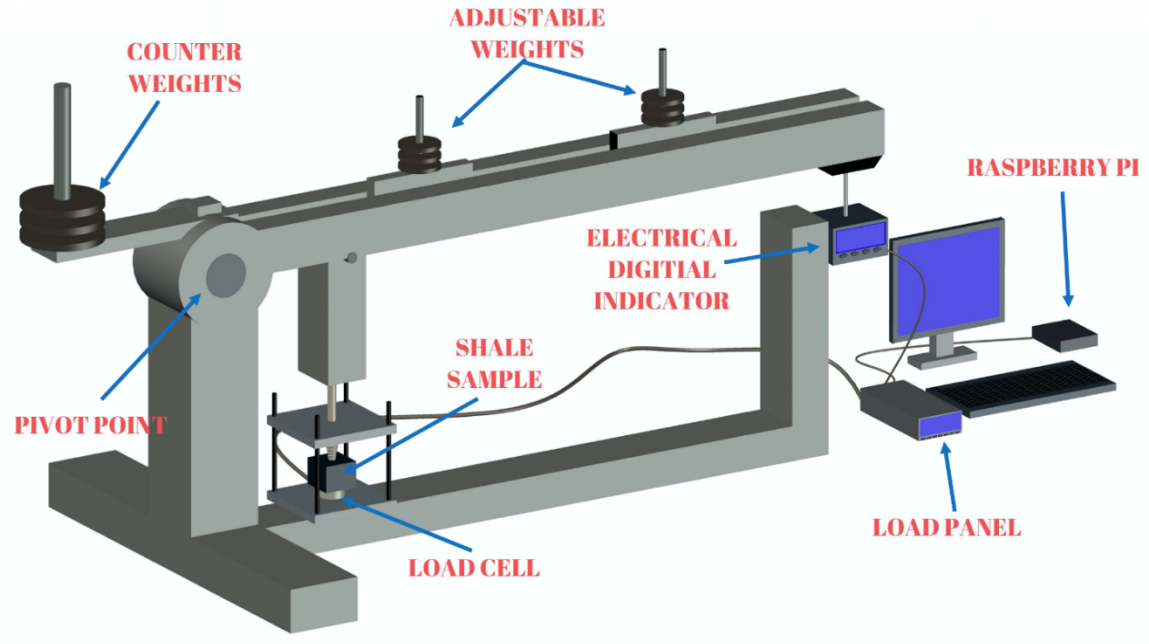

Figure 14. An AutoCAD software view of the experimental setup for the load-controlled test (not to scale)

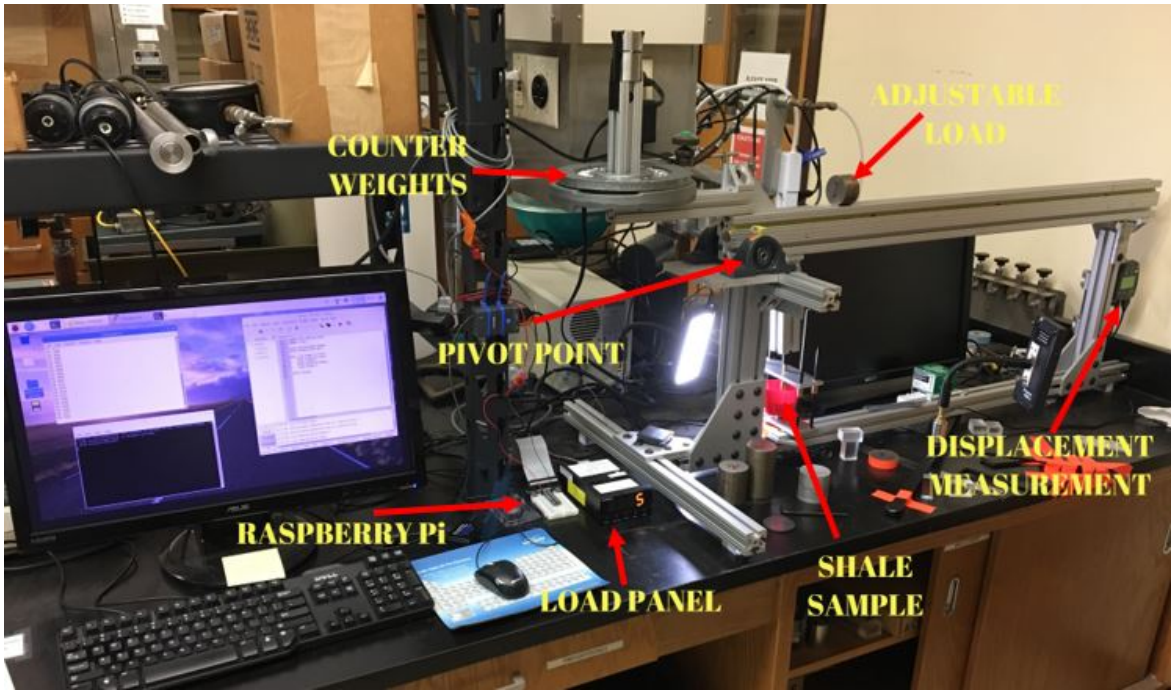

Figure 15. A photo of the experimental setup for the load-controlled test

1) Adjustable Loads – Various metal weights are used on the rigid frame to adjust the load. These loads are checked regularly to ensure it remains constant.
2) Tungsten Carbide Ball – 1 mm diameter indenter (spherical ball) represents a proppant. The indenter and surrounding area are kept fully saturated with the fracturing fluid.
3) Shale Sample – Preserved Utica Shale samples were used in these tests, and they are kept wet throughout the tests.
4) Miniature Load Cell – 0.75 in diameter load cell measures the force.
5) Load Panel Meter – This panel displays the force applied on the miniature load cell.
6) Electronic Digital Indicator – An electronic device is used as a displacement measurement of the shale sample during tests.
7) Raspberry Pi (R-Pi) – A microcomputer controls the data acquisition and recording. R-Pi tells the displacement gauge (electronic digital indicator) to send out a measurement at set time intervals. For all tests, this time interval was set as 2 seconds. The R-Pi records the data and timestamps every entry for later analysis.
8) Pivot point – It reduces the friction of the rigid frame arms.

3.2.2 Displacement Controlled Test

The second experimental setup is a displacement-controlled test. The displacement-controlled apparatus was built to quantify elastic and plastic deformations separately. Also, time-dependent rock deformation, which refers to creep, proved to be negligible since this set up was designed for quick tests that usually lasted less than a minute. Figure 16 shows a schematic of the displacement-controlled test; the main element is a high precision screw with 80 threads per inch,

which is twice as accurate as a micrometer. Each degree of rotation of the screw translates to less than 0.0009 millimeters of linear motion. The rotation is decoupled from the displacement by a high length-to-diameter ratio (l/d) screw adapter sleeve, the combination of close diameter matching tolerance with the precision screw, and the high l/d ratio minimizes any angular displacement. An indicator pin attached to the precision screw projects radially out to a position just above a printed protractor; this allows for precise angular positions are obtained. A precision load cell is located underneath the shale sample to measure transmitted load through the shale. With the combination of displacement and load data, elastic-plastic load curves are relatively easy to generate.

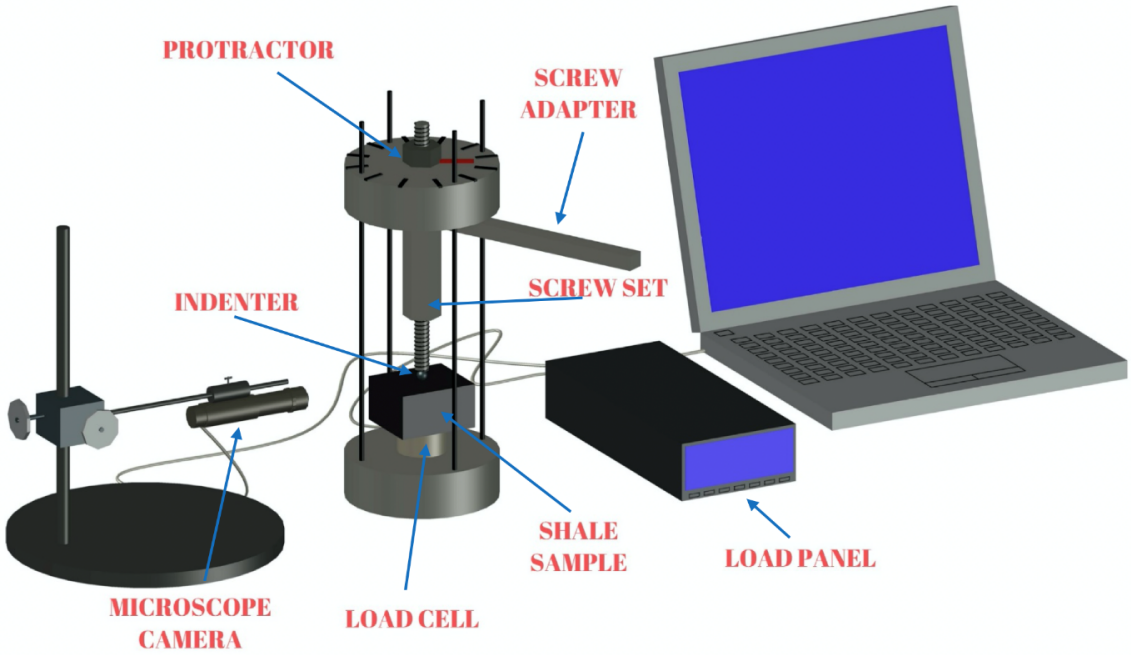

Figure 16. An AutoCAD software view of an experimental setup for the displacement-controlled test (not to scale)

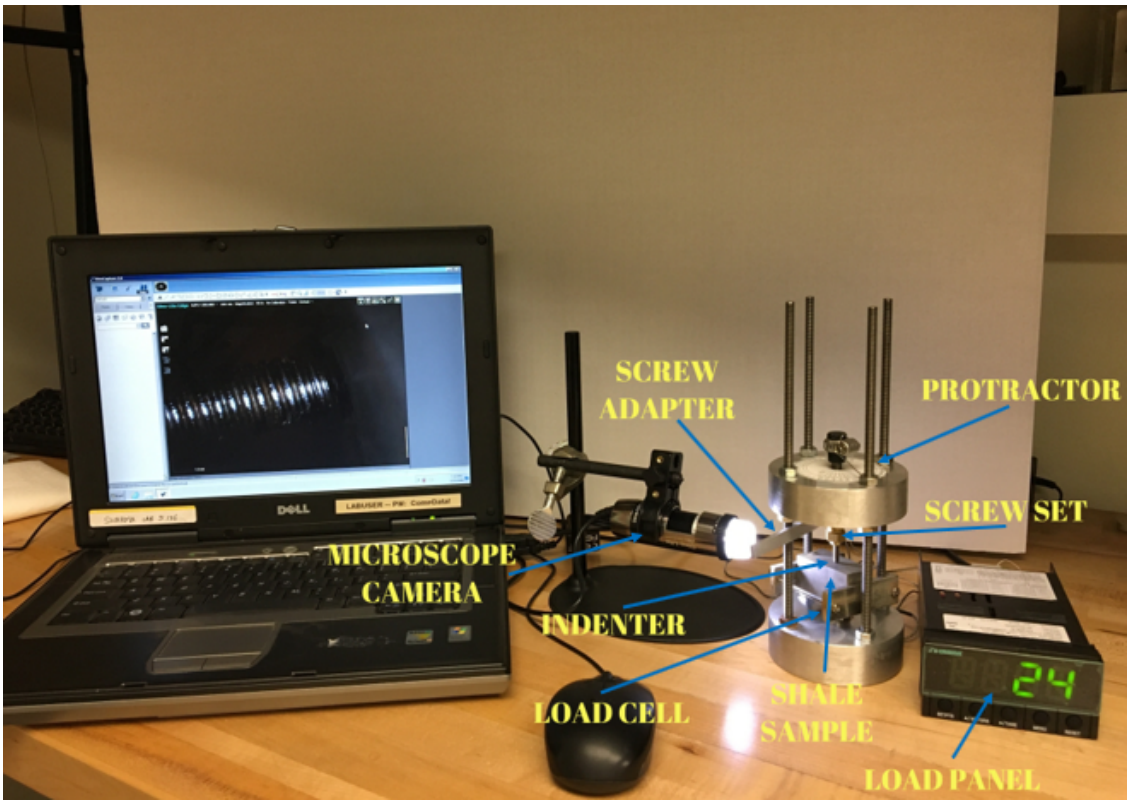

Figure 17. A photo of experimental setup for the displacement-controlled test

1) 7 mm (optical bench) precision adjustment screw – Turning the screw drives the indenter into the shale sample. The precision (0.25 in. diameter, 80 threads per inch) optical bench screw controls the displacement by controlling the screw rotation. The precision screw linearly displaces 0.0125 in (0.3175 mm) per revolution. Making it two times more sensitive than a standard micrometer screw.
2) Proppant Load Frame Assembly – Similar versions were built for both load-controlled and displacement-controlled tests. In the displacement test, the frame is fixed in place, and the screw moves down. In the load test, the screw is fixed in place, and the whole upper frame section moves down.
3) Microscope Camera – This microscope camera images the embedment during the test. A sample photo can be found in Appendix G.

4) Screw Adapter – It separates the rotation of the precision screw from the linear displacement of the indenter.
5) Protractor - This enables the precision measurement of the turning angle.
6) Tungsten Carbide Ball – 1 mm diameter tungsten carbide spherical indenter represents a proppant particle. During the tests, the proppant (indenter ball) and surrounding area are kept fully saturated with the fracturing fluid.

Figure 17 shows a photograph of the actual experimental setup. As with the load-controlled test, the displacement test apparatus was calibrated using a range of material standards in order to obtain the elastic response of the displacement apparatus itself. Since the amount of displacement in this test is tiny, a very hard high-density Titanium Diboride (TiB_2) precision ground optically flat and highly parallel ceramic disc was used in the displacement-controlled test in order to calibrate the assembly's contribution to the deformation measurements. This ceramic (TiB_2) disc is an extremely hard material with a 190 GPa modulus and a hardness of 27000 MPa, and even a tungsten carbide indenter cannot penetrate it. By testing the apparatus with the ceramic, the mechanical response of the proppant load frame assembly, including the load cell itself, is measured and subtracted from the experimental results for accuracy. The TiB_2 ceramic standard was tested periodically to ensure the assembly's integrity and as shown in Figure 18.

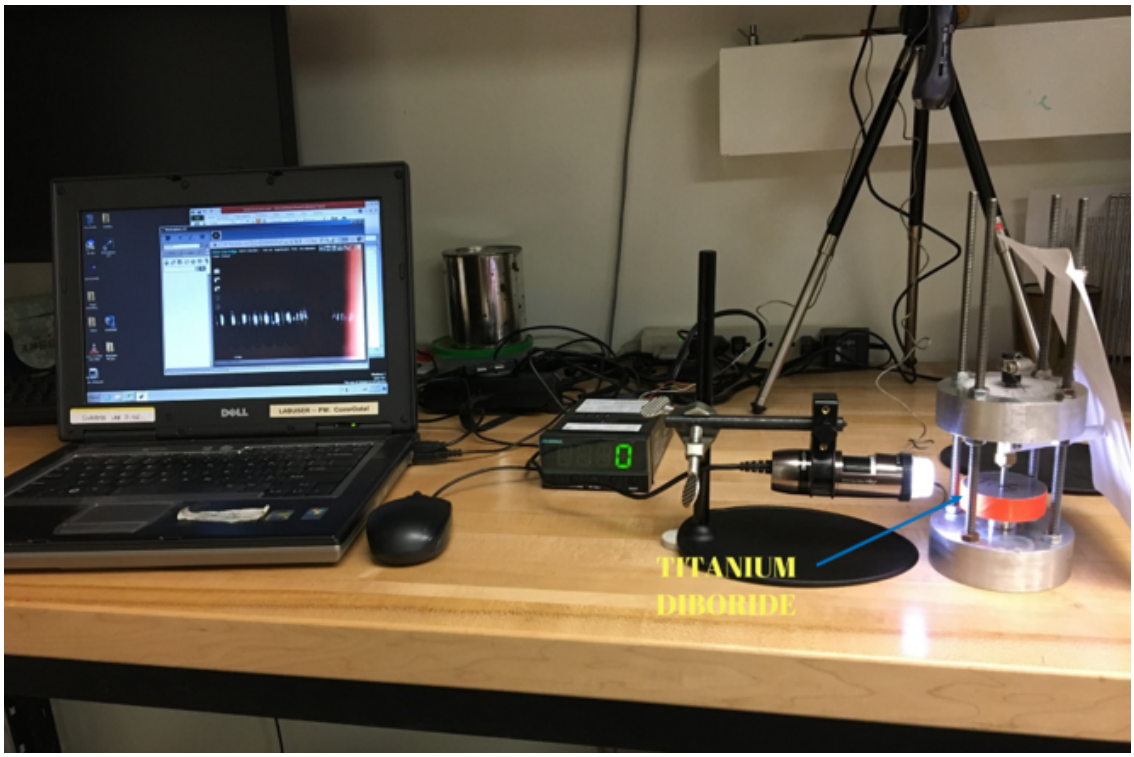

Figure 18. A photo of the TiB_2 experiment.

3.3 Shale Sample and Fracturing Fluid Preparation

Fluids used in the testing were prepared using these methods and controls.

1) Shale samples were cut into approximately 1-inch cubes from the same preserved Utica Shale Core.
2) Different fracturing fluids were mixed for 1-2 minutes in a high shear rate blender with minimum air entrainment.
3) After blending, the fluids rested for 1 hour in a sealed beaker.
4) The shale sample cubes were soaked in sealed containers of the various fracturing fluids for 15 days.
5) The shale samples were tested in both the load-controlled and displacement-controlled test apparatus in sequence.

6) Once a shale sample was exposed to a fracturing fluid, it was kept wet with its fracturing fluid throughout all the tests and storage periods.

3.4 Mineralogy

The shale elemental composition was determined by an energy-dispersive x-ray fluorescence (ED-XRF) spectrometer (Bruker, Tracer IV-SD). Figure 19 displays a photo of the spectrometer. First, the spectrometer sampled an empty chamber to record a baseline spectrum without shale. The shale samples analyzed using the XRF (15 kV, 40 μA, tube vacuum on, 60 seconds), the spectral data were plotted, and the elements were recorded using S1calprocess software.

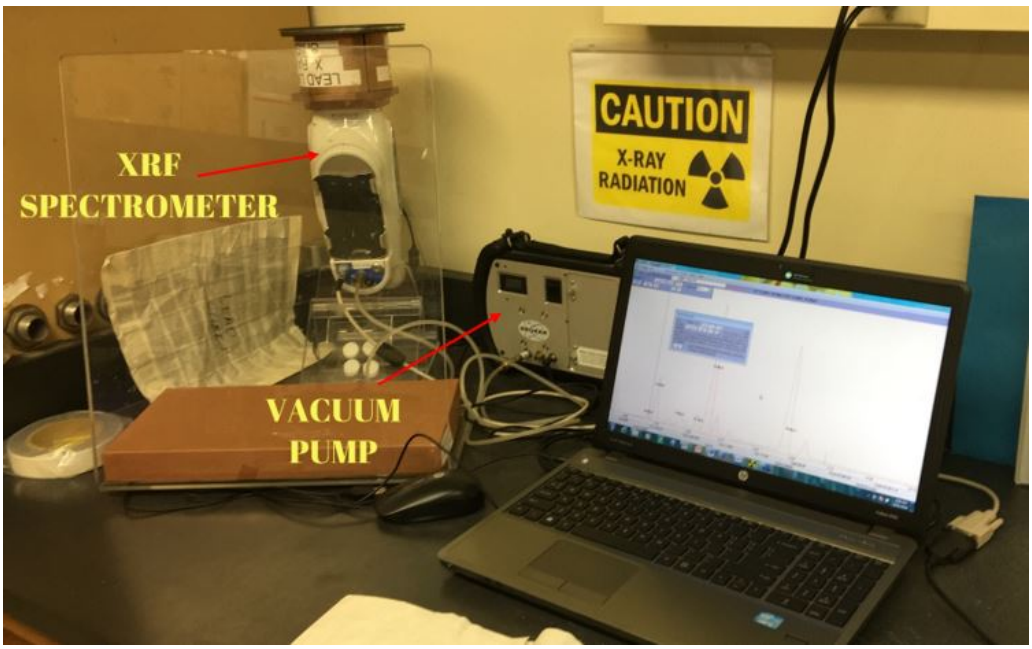

Figure 19. X-Ray fluorescence spectrometer.

Then the relative abundance of minerals was scaled to the average element concentrations measured, and clay content estimates were made by making the following assumptions:

1) Aluminum (Al) is found only in clay, and clay consists of kaolinite and illite minerals.

2) The fraction of the Aluminum is equal in both kaolinite and illite.
3) Calcium (Ca) is found in calcite and dolomite.
4) Silicon (Si) is present in both quartz and clay.

More detailed calculation steps and equations can be found in Appendix F.

Chapter 4: Theory and Developed a Mathematical Model[2]

4.1 Background Theory

Understanding the proppant embedment mechanism is essential for hydraulic fracturing treatments. Proppant embedment can be considered as a hard, grainy material indenting into a rock surface. Rock indentation has been studied extensively in rock engineering, including the oil & gas drilling process for decades (Nelson, Ingraffea, and O'Rourke, 1985; Lawn and Wilshaw, 1975; Tan, Kou, and Lindquist, 1996; Alhossein and Hood, 1996; Kou et al., 1995; Kutter and Sanio, 1982; Wijk, 1989). Rock indentation is the method that provides the most basic information about mechanical rock failure. Thus, rock indentation physics was used for this project.

There are many studies on the subject in the past. The models employed for indentation test data analysis were that of Hertz, 1863., Pharr et al., 1991., and Tabor, 1951. From the displacement-controlled test, a typical indentation load-displacement plot can be obtained. Figure 20 shows the schematic of load-displacement data. The unloading slope gives stiffness (S) which can be written as

$$S = \frac{dP}{dh} \tag{4.1}$$

where P is the applied load, and h is the displacement.

[2] The content of this chapter was published as: Alagoz, E., Wang, H., Russell, R. T., & Sharma, M. M. (2020, September 18). New Experimental Methods to Study Proppant Embedment in Shales. American Rock Mechanics Association.

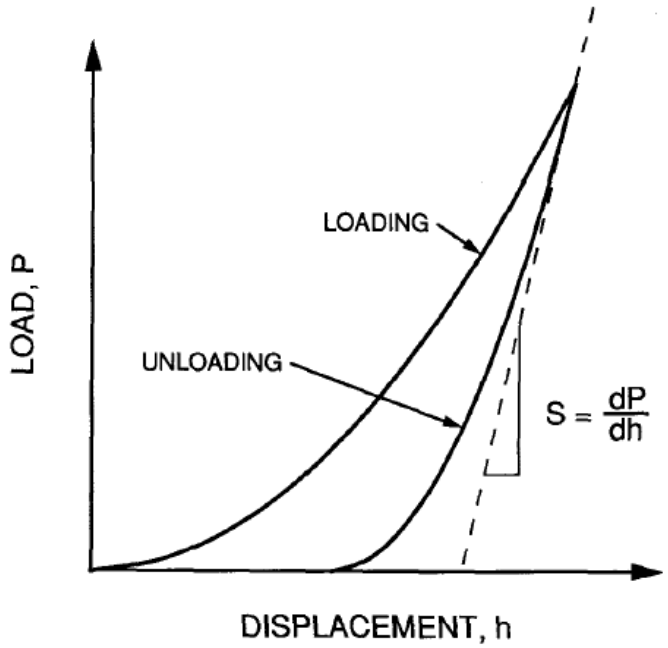

Figure 20. Example of load-displacement data. (From Pharr et al., 1991)

Sneddon, 1965 stated a simple relationship between load and displacement. From Sneddon's analysis, the relation between load(P) and displacement(h) can be formulate by the following equation where a is the indenter radius, μ is the shear modulus, and ν is the Poisson's ratio.

$$P = \frac{4\mu a}{1-\nu} h \tag{4.2}$$

Since spherical ball (1 mm tungsten carbide) was used as an indenter, the projected area of the ball (area of the contact circle) is simply:

$$A = \pi a^2 \tag{4.3}$$

By recalling the elastic modulus through equation 4.4, Sneddon's analysis leads to equation 4.5 where $E_r = E/(1-\nu^2)$ expressed the reduced modulus, E is the Young's modulus and ν is the Poisson's ratio of the shale sample.

$$E = 2\mu(1+\nu) \tag{4.4}$$

$$E_r = \frac{\sqrt{\pi}}{2}\frac{s}{\sqrt{A}} \tag{4.5}$$

Therefore, it can be seen from here that the elastic module can be calculated from the load-displacement plot obtained at the end of the displacement-controlled test.

Existing mechanical studies were considered to express the relationship between indentation stress and strain mathematically. The first analysis of a spherical body indenting an elastic half-space was done by Hertz, 1863. Figure 21 illustrates the parameter used in the calculations where F is the applied load, a is the contact radius, R is the radius of the indenter, and h_c is the contact depth.

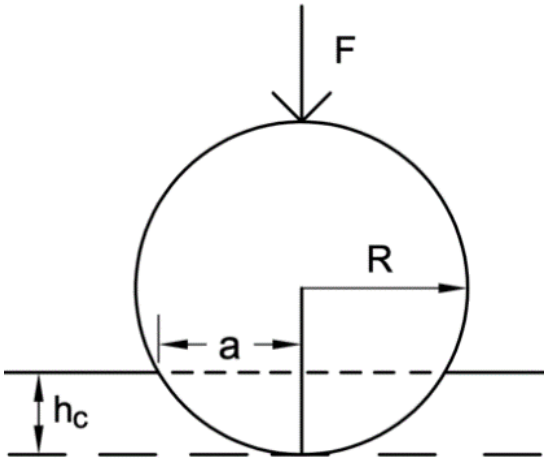

Figure 21. The geometry of spherical indentation. (From Alagoz et al., 2020)

The relation between contact depth and contact radius can be written as

$$a = \sqrt{2Rh_c - h_c^2} \tag{4.6}$$

Oliver-Pharr model (Pharr et al., 1991) gives the contact depth by the following expression where ε is the geometric constant and is 0.75 for a sphere (Herbert et al., 2001).

$$h_c = h - \varepsilon \frac{P}{S} \tag{4.7}$$

Indentation stress and indentation strain are defined as

$$\sigma_{ind} = \frac{P}{\pi a^2} \tag{4.8}$$

$$\varepsilon_{ind} = \frac{a}{R} \tag{4.9}$$

In Tabor's approach, the indentation strain was further invoked to be $0.2 \cdot a/R$, where the strain pre-factor of 0.2 was determined empirically. Therefore, indentation stress-strain relation in the elastic region can be expressed by the equation 4.10. Figure 22 displays the sample data of the displacement-controlled test.

$$\sigma_{ind} = 0.2 E_r \varepsilon_{ind} \tag{4.10}$$

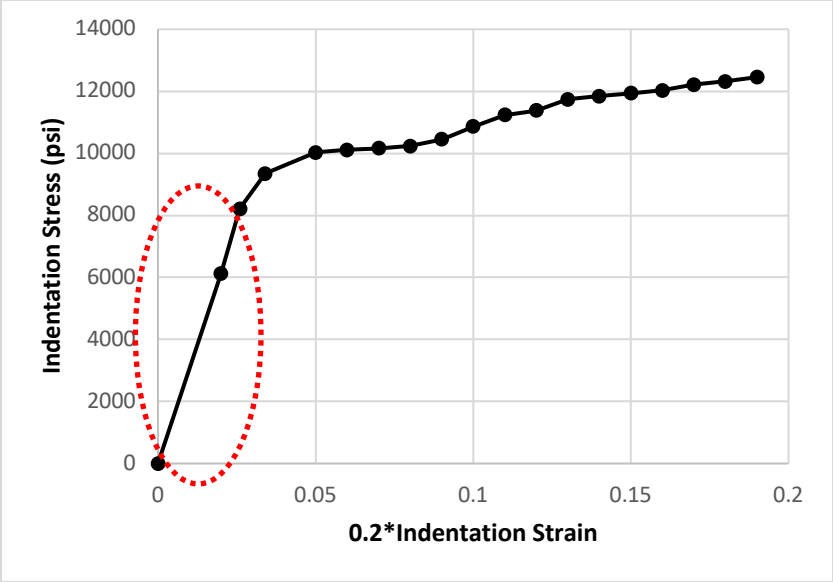

Figure 22. Indentation stress-strain relation, displacement-controlled data. (From Alagoz et al., 2020)

Meyer (1908) showed a power-law relationship that relates the charge (P) to the radius (a) of the indentation.

$$P = B(2a)^{\mu} \tag{4.11}$$

where B and μ are empirical parameters. Tabor (1951) showed that a relationship between μ and m can be established using the power-law function of strain.

$$\sigma = K\varepsilon^{m} \tag{4.12}$$

where

$$m = \mu - 2 \tag{4.13}$$

In Figure 23, by plotting load versus indentation stress and indentation strain K and m parameters can be obtained.

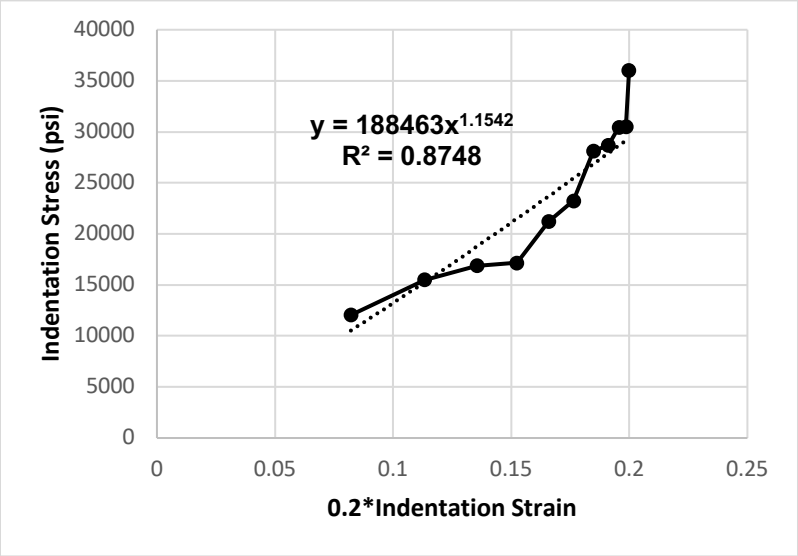

Figure 23. Indentation stress-strain relation in the plastic region. (From Alagoz et al., 2020)

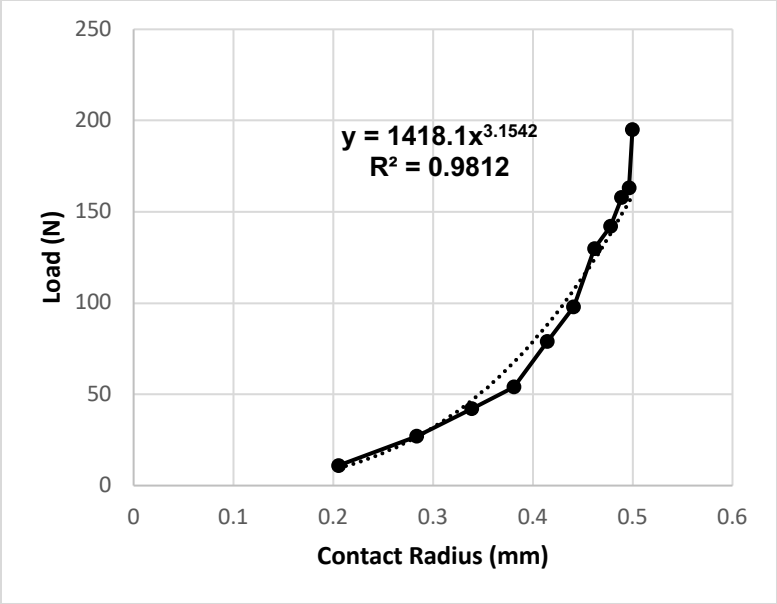

Figure 24. Load-contact radius relation in the plastic region. (From Alagoz et al., 2020)

B and μ obtained from the Load-contact radius plot in Figure 24, and experiments were kept repeated until the equation 4.13 satisfied.

4.2 Developed Model

The elastic-visco-plastic model that has been developed for deformation calculations (equation 4.14 and equation 4.15) can be used for stress-dependent deformations in both elastic ($\sigma < \sigma_{yield}$) and plastic ($\sigma > \sigma_{yield}$) regimes. Since the displacement-controlled test (fast test) prevents creep from occurring, these two deformations can be calculated from this test. ε_e, ε_p, and ε_c are the elastic, plastic, and creep strain, respectively.

$$\varepsilon_e = \frac{\sigma}{E_r} \tag{4.14}$$

$$\varepsilon_p = \left(\frac{\sigma}{K}\right)^{\frac{1}{m}} \tag{4.15}$$

On the other hand, the load-controlled test has been used to measure total deformation, including elastic, plastic, and creep. Elastic and plastic deformation contributions can be calculated

from the displacement-controlled test by using equation 4.14 and equation 4.15. Total deformation curve obtained from the load-controlled test. Subtracting these stress-dependent deformation components from the total curve leaves only the deformation caused by creep. By fitting the power-law model to this residual data, the empirical parameters C and n are obtained. Then creep deformation can be described by the following equation.

$$\varepsilon_c = Ct^n \tag{4.16}$$

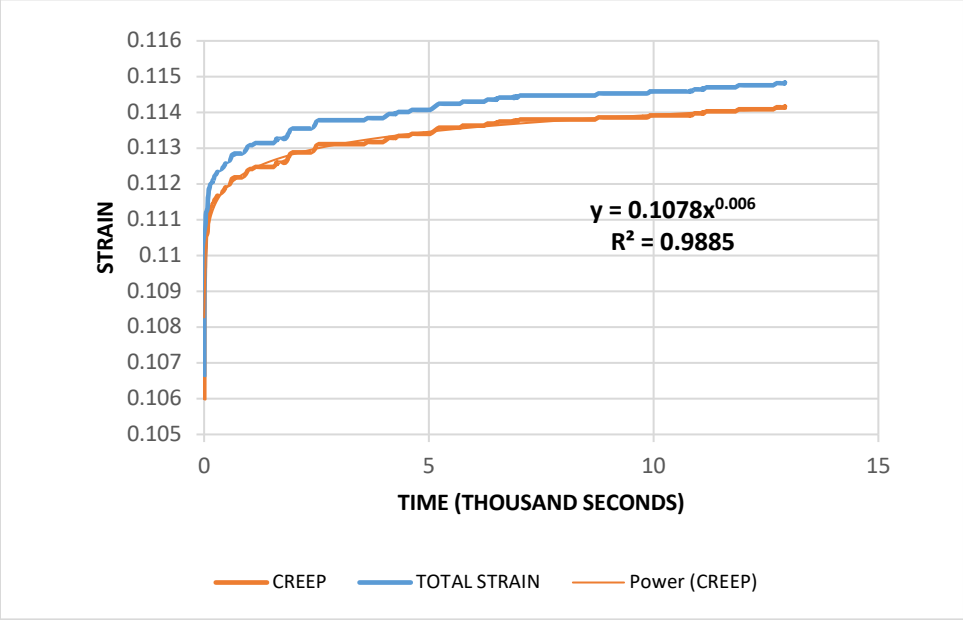

Figure 25. Load-controlled test data. (From Alagoz et al., 2020)

Equation 4.14, 4.15, and 4.16 combine to form the total deformation in the following relationship:

$$\varepsilon = \frac{\sigma}{E_r} + \left(\frac{\sigma}{K}\right)^{\frac{1}{m}} + Ct^n \tag{4.17}$$

Rock deformation behavior can be split into its elastic, plastic, and creep components by using the model in equation 4.17.

Chapter 5: Results and Discussion

The main results from our experiments and their interpretation using our models are summarized in this chapter.

5.1 Effect of Mineralogy

High clay-content shale samples generally experience severe proppant embedment with significant fracture conductivity reduction (Alramahi and Sundberg, 2012). Four Utica shale samples with different mineralogy were selected and soaked with the same fracking fluid and tested to address the effect of shale rock mineralogy on proppant embedment in this work. The mineralogy content of the shale samples can be found in Appendix F. The results show a positive correlation between proppant embedment and the clay content of the shale.

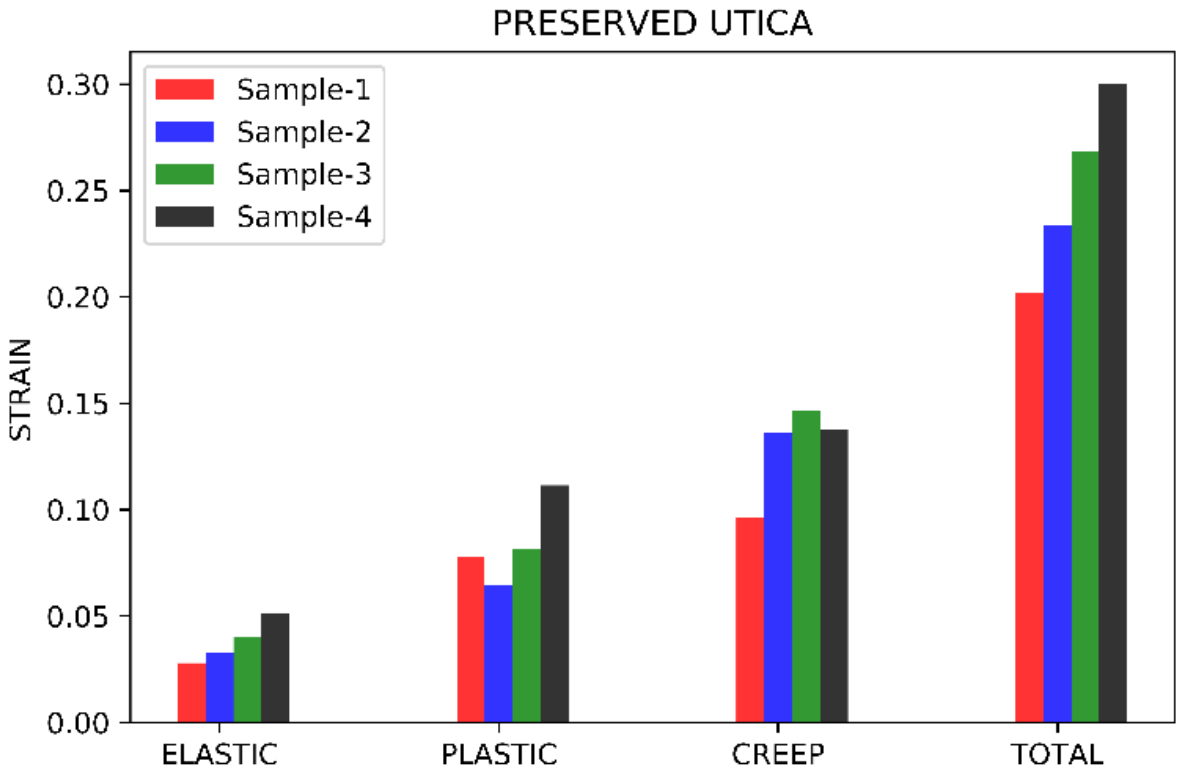

Figure 26. Preserved Utica Shale sample embedment results. (From Alagoz et al., 2020)

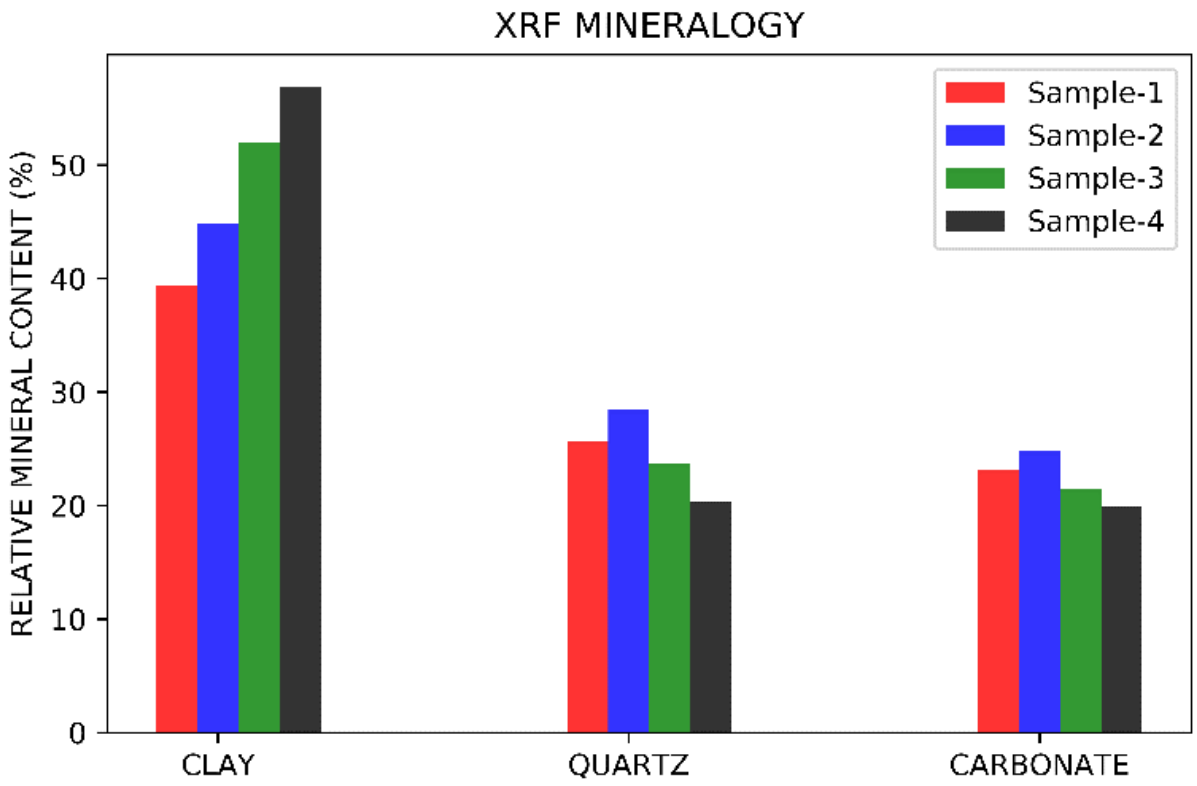

Figure 27. The mineralogy of preserved Utica Shale samples. (From Alagoz et al., 2020)

As can be seen from Figure 26 and Figure 27, the higher clay content in the shale leads to larger strain values; in other words, more deformation, and therefore, more embedment. It can also be seen from the deformation data that elastic deformation is 5-15 percent of the total deformation. Therefore, shale deformation is mostly dominated by plasticity and time-dependent creep.

5.2 Time Dependence

It is important to note that if the penetration depth of the 1 mm tungsten carbide indenter is deeper than the invasion distance of the fracturing fluid, then the data recorded is not reliable when comparing the fracturing fluid effect on the embedment. Therefore, it is necessary to determine the soaking time versus soaking depth in the shale samples for each fracturing fluid.

A technique was developed for this calculation. Firstly, Nuclear Magnetic Resonance (NMR) was used to determine the liquid volume in the shale sample before soaking. Then, the

shale sample was soaked in a fracturing fluid for five days; after this soaking time, another scan NMR was performed, and the liquid volume was read from the NMR result. This cycle was repeated every five days for fifteen days, and the imbibed liquid volume in the shale rock was progressively recorded. By assuming uniform penetration, the invasion depth of fracturing fluid was calculated from the following equation 5.1, and the results are tabulated in Table 2.

$$\Delta V = hA\Phi \tag{5.1}$$

Where ΔV is the differential volume, which is read from NMR results, h is the invaded depth, Φ is the porosity, and A is the surface area of the shale sample. Since the liquid volume imbibed by the shale sample is small, the surface area of the shale sample was determined with another precise calculation. A shale sample was positioned on a known scale (graph) paper, and a photograph of each face of the shale sample was taken with a high-quality telephoto camera from a far distance. This photography technique eliminates parallax distortion, and angular ray magnification since all point source (camera) rays are parallel at infinity, and the angular distortion is governed by the Tan Ø ≈ Ø approximation at long distances. Photo analysis using Gimp software provided a simple pixel per inch conversion for each picture, and the overall surface area of each shale sample was calculated by summing the six faces of the cube.

Table 2. Liquid Volume for after each NMR test was performed

Duration	**Liquid Volume (mL)**	**ΔV (mL)**	**h (mm)**
Initial	0.369	0	0
5 days	0.404	0.035	0.236
10 days	0.425	0.056	0.378
15 days	0.438	0.069	0.466

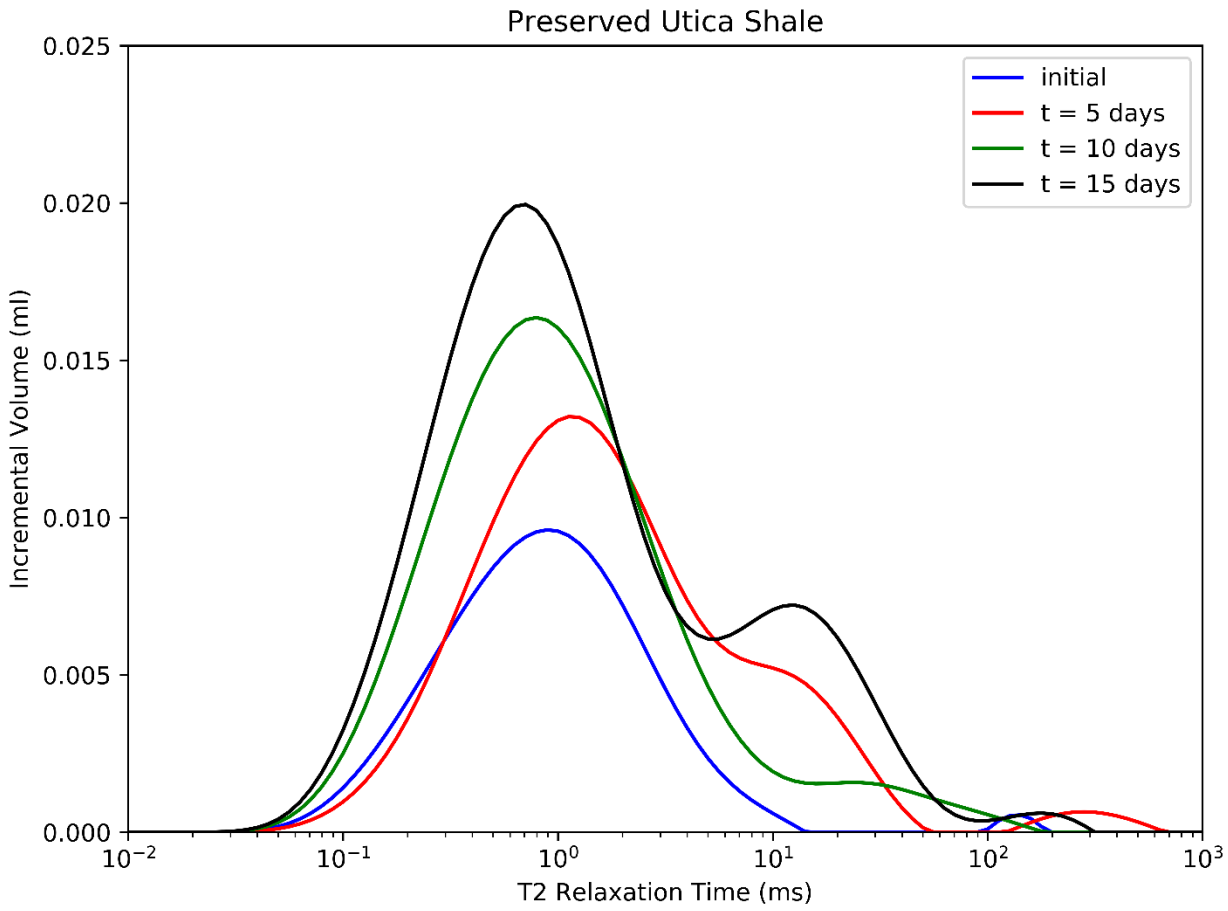

Figure 28. NMR results for penetration depth calculation.

Figure 28 shows the NMR results of a preserved Utica shale, and it shows the clear correlation between soaking time and the volume of soaking liquid. Table 2 shows the liquid volume in the shale after each soaking period. Based on the penetration distance calculation results, samples were exposed to the fracturing fluid for 15 days. In both experiments, a 1 mm diameter tungsten carbide ball has been used to represent a proppant grain. The maximum embedment depth in this study is 0.5 mm, which is equivalent to the ball radius. However, the data selected from the experiments and used in this paper are for embedment of less than 0.466 mm in order to see the effect of the fracking fluids more accurately.

5.3 Effect of Fracturing Fluid

The shale samples were tested after being exposed to different fracking fluids to see how the fluids would mitigate embedment. Different combinations of chemicals were tested to understand the interactions among fracking fluids and the shale. Some of the tested fluids are listed in Table 3. The fluids named on the graphs are the imbibed fracturing fluids by the shale samples tested.

Table 3. List of Fluids Soaked by the Shale Samples and Their Fraction

Fluid	**Name**	**Concentration in Fluid**
DI	Deionized Water	Base Fluid
KCI	Potassium Chloride	3 %
FR1	Friction Reducer 1	0.1 %
FR2	Friction Reducer 2	0.1 %
CI	Clay Inhibitor	0.1 %
S7	Surfactant 7	0.1 %
S8	Surfactant 8	0.1 %

5.3.1 Fluids Combination in DI Water Without Surfactant

In this set of test results, different fracturing fluids mixed in a deionized water (DI) solution were compared in terms of their effect on the proppant embedment. Figure 29 shows the embedment results seen in the shale samples tested; in the plotted data, taller bars have more embedment. While the least amount of embedment was obtained when the shale samples were soaked in DI 3% KCl solution, the sample soaked in the DI 0.1% clay inhibitor (CI) solution resulted in the worst embedment. Friction reducers 1 and 2 mitigated the embedment somewhat compared to the deionized water baseline. The Surfactant 7 (S7) solution did not make a measurable difference when using it alone. Nonetheless, S7 had other positive properties important enough to conduct a series of tests to see if it could be made to help with embedment.

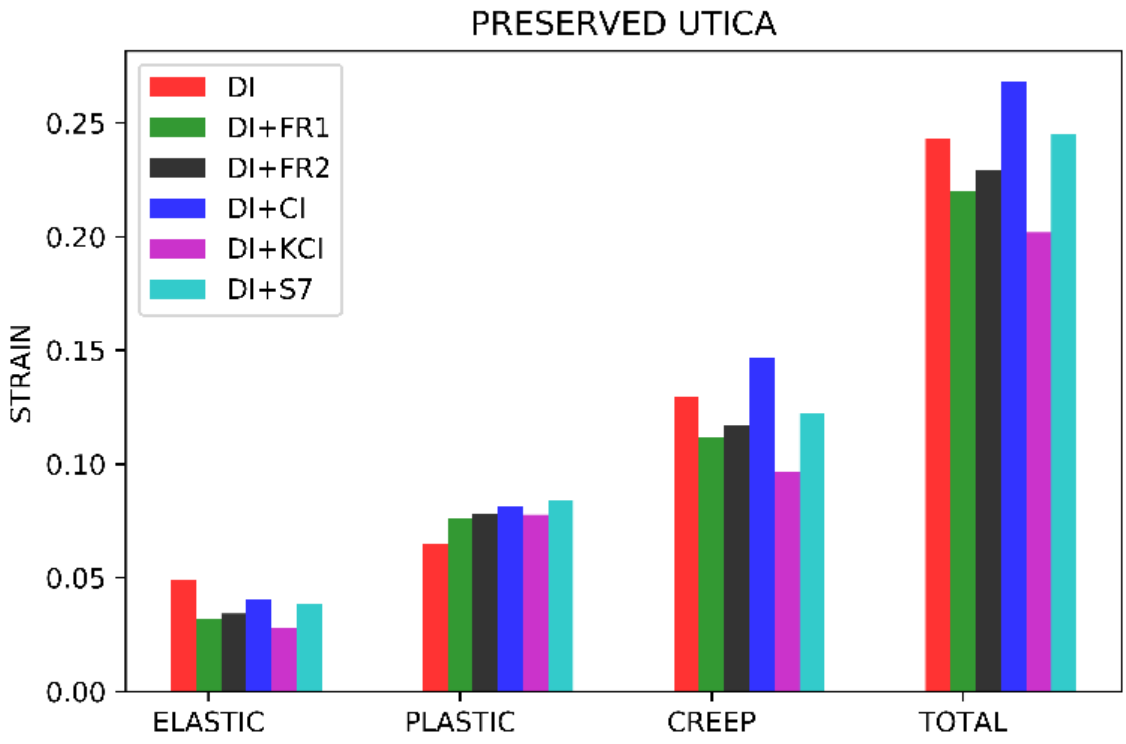

Figure 29. Deformation of different fracturing fluids in deionized water. (From Alagoz et al., 2020)

5.3.2 Surfactant-Based Fluid Combination

S7 based fracturing fluids were studied in these tests; all the solutions started with a (DI 0.1% S7) composition to which other frac-fluid chemicals were added. The results of these tests are shown in Figure 30: the red bar represents shale deformation in the samples soaked with the S7 base fluid. The addition of clay inhibitor to the S7 solution (blue bar) yielded the best result, followed by the S7 plus KCl brine solution. As noted, the dominant modes of shale deformation are plasticity and creep, and the addition of clay inhibitor to the fluid dramatically reduced the plastic deformation.

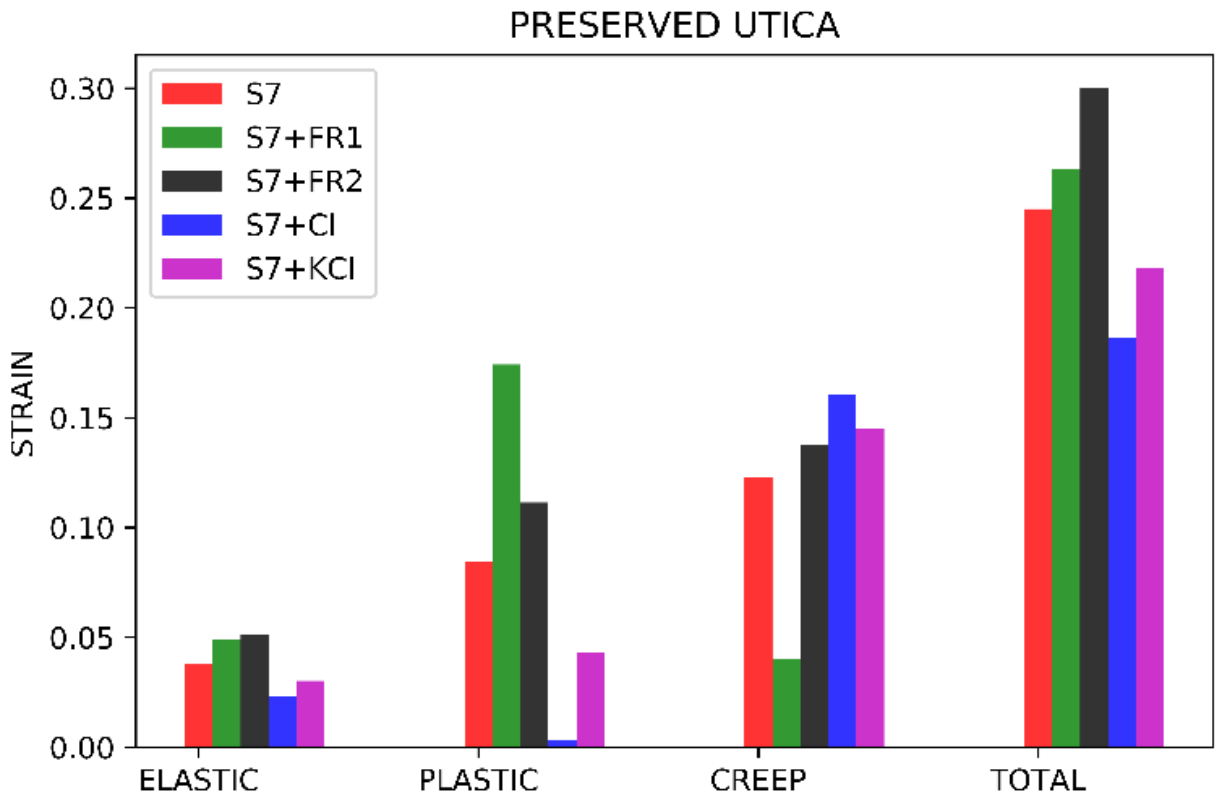

Figure 30. Deformation of different fracturing fluids with Surfactant 7. (From Alagoz et al., 2020)

5.3.3 Brine-Based Fluid Combination

The base fluid, in these tests, is deionized water (DI) plus 3% KCl. Figure 31 depicts the embedment results of shale samples after being soaked in various KCl based solutions. The least amount of embedment is measured for the sample soaked in 3% KCl only. While fluids other than Clay inhibitor increase embedment, Clay inhibitor with 3 % KCl made a slight increase in the embedment.

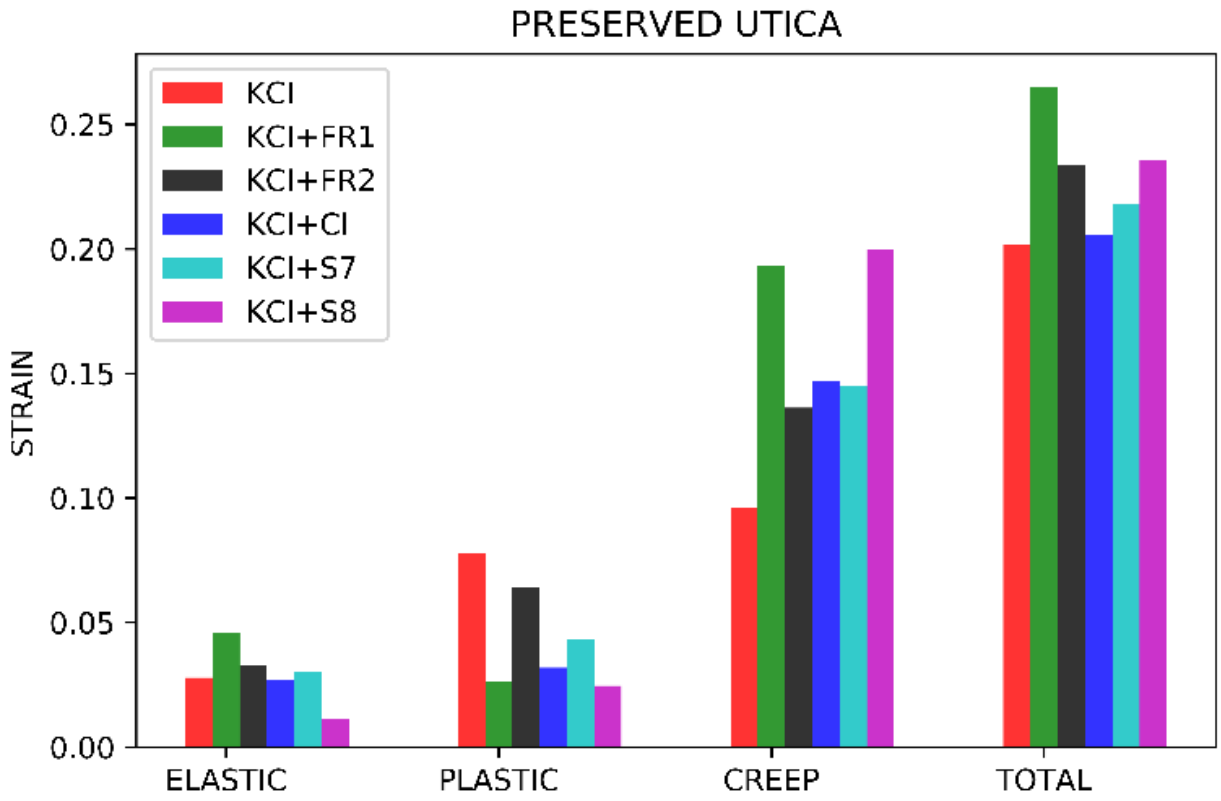

Figure 31. Preserved Utica Shale sample deformation test results. (From Alagoz et al., 2020)

5.3.4 Surfactant-Brine-Based Fluid Combination

In these tests, fluids combining Surfactant 7 (S7) and KCl as the base fluid were tested with other fracturing fluid additives. Figure 32 shows the embedment test results of shale samples after being soaked in KCl based chemicals. Although S7+KCI (green bar) reduces the plastic deformation of the shale, it increases the creep deformation, which results in a higher total deformation. S7+KCl+Cl mitigated embedment better than the other fracking fluid combinations.

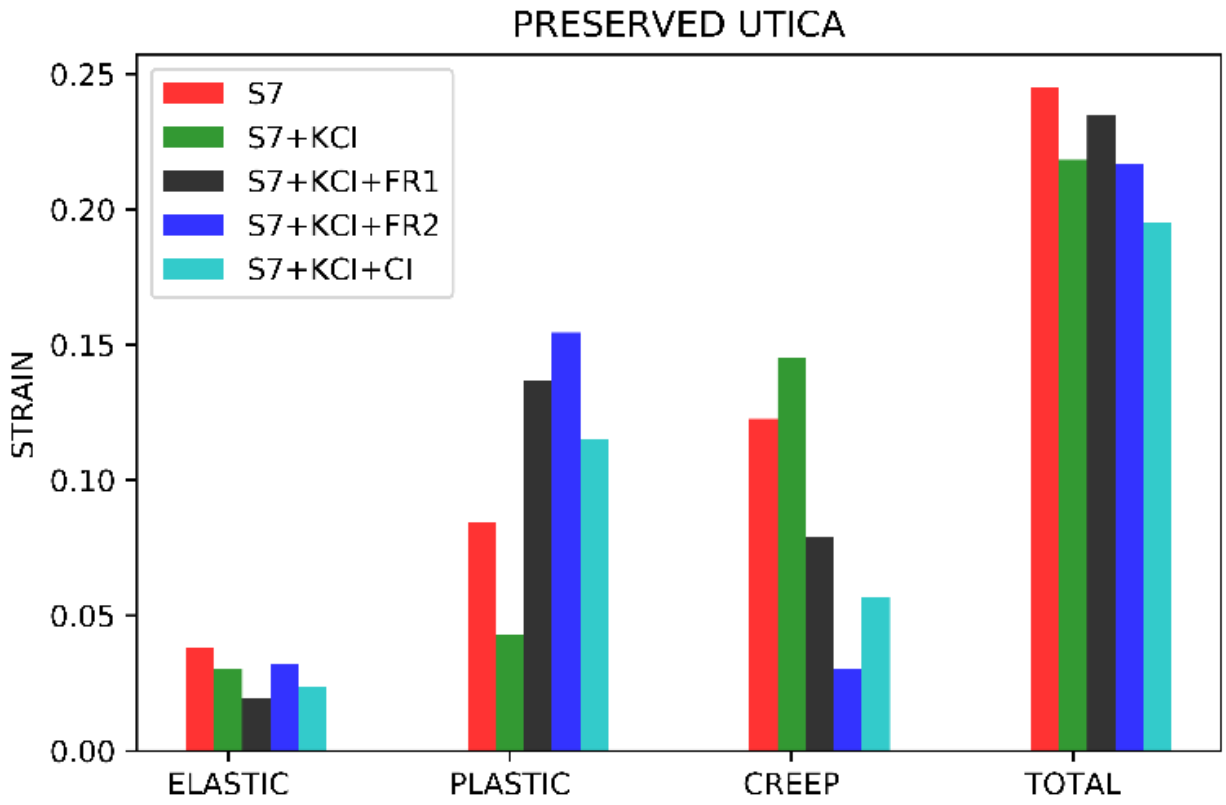

Figure 32. Preserved Utica Shale sample deformation test results. (From Alagoz et al., 2020)

Chapter 6: Conclusions and Recommendations for Future Work

6.1 Conclusions

Many interrelated problems can result in a rapid reduction in the productivity index, such as proppant embedment, proppant crushing, fines migration, and clay swelling. Since a 1 mm tungsten carbide spherical ball was used in these experiments, the effect of proppant crushing was eliminated from the study. Fines generation, and clay swelling are also beyond the scope of this research. Proppant embedment, however, plays a significant role in the reduction of fracture conductivity and, consequently, a rapid decline in the productivity index. This study primarily focused on understanding the proppant embedment mechanisms combined with the fracturing fluid effects on the embedment as well as how both factors interacted with shale mineralogy. Two main mechanisms will lead to severe proppant embedment reservoir depletion and time. Firstly, reservoir depletion, which increases the effective closure stress, will contribute to the stress-dependent elastic and plastic deformations. As stated previously, plasticity is the dominant proppant embedment path in shale deformation. Therefore, the main reasons for severe proppant embedment can be considered a combination of high effective stresses and depletion time. Creep, time-dependent deformation, also increases the embedment during production. Additionally, shale mineralogy, combined with water-based fracturing fluids, also contributes to the overall proppant embedment. Proppant embedment can be worse in clay-rich (low stiffness) shales with some fracturing fluid combinations. The following findings were listed regarding indentation tests:

- A set of constitutive equations was developed to account for elastic, plastic, and creep deformation during proppant embedment. Also, the parameters used in this model can readily be obtained from laboratory tests.

- Two new experimental apparatuses were developed and used to quantify the shale rock/proppant deformation behavior (elastic, plastic, and creep) after exposure to various fracture fluid additives such as surfactants and clay stabilizers.
- Embedment measurements were made and reported for constant displacement and constant load conditions; the combination of these tests allows for the separate measurement of the elastic, plastic, and creep components of shale deformation.
- Proppant embedment primarily occurs due to plastic deformation followed by time-dependent creep deformation into the shale. The initial elastic deformation is small.
- Fracturing fluid chemistry affects the amount of plastic deformation and creep substantially.
- The role of rock mineralogy combined with fracturing fluid chemistry on embedment was studied. Higher clay content in the shale sample leads to more severe proppant embedment and more substantial plasticity.
- Chemical treatments fostered the best improvements in high clay shales.
- Chemical additives such as clay inhibitors in deionized water can, in some cases, cause more deformation. However, when it is used in conjunction with other surfactants (such as surfactant 7), the amount of embedment decreased.
- The experimental techniques developed in this study can be quickly used to evaluate the impact of several frac fluids on proppant embedment.

- The measurements from these two experimental setups can be used as input parameters to predict fracture conductivity and help to optimize fracturing fluids, proppant size, and proppant type.
- With given stresses, strain and deformation can be calculated. Thus, updated fracture width can be obtained, and from that, fracture conductivity can be computed.

6.2 Recommendations for Future Work

There is further research to be done on this topic. These experiments were conducted manually in the lab. The next step would be working on the automation of these two experiments and data acquisition simultaneously. Once this is done, these experimental apparatuses can be re-built in a more compact setup. Moreover, these experiments were conducted at ambient pressure and temperature conditions. Generalization and stabilization at reservoir conditions were not studied in this research. Thus, in any further study, a more extensive range of parameters would undoubtedly improve the generalizability of the results, and the following step would be to perform these embedment tests at reservoir conditions. This would allow for a better application of these experimental findings in the field.

Furthermore, proppant embedment increases with production time. Hence, fracture conductivity cannot be maintained for a long time, and it will gradually decrease. This means re-fracturing is required after a period of production time if the production rate is desired to be sustained. In the stimulation of permeability challenged shale reservoirs, measures should be taken to mitigate proppant embedment. Firstly, to reduce the weakening of the rock, fracturing fluid additives should be optimized. Secondly, to reduce exposure time, operation procedures should be

reviewed to eliminate time losses. These are recommendations, but local field experience and reservoir parameters should determine specific procedures.

Appendix A

PYTHON codes to obtain displacement data continuously from the creep test. These codes are used in the Raspberry Pi, a microcomputer.

```
#first import the GPIO libraries, and time
import RPi.GPIO as GPIO
import time
#set up the GPIO PIN here, check the board.
GPIO.setmode(GPIO.BOARD)
GPIO.setup(5,GPIO.OUT)
#set up the output pin number and time, in this case we take the data
every 5 seconds
for x in range (0,100000):
    GPIO.output(5,True)
    time.sleep(5)
    GPIO.output(5,False)
    time.sleep(5)
GPIO.cleanup
```

Appendix B

PYTHON codes to generate NMR T_2 distribution curves.

```
import pandas as pd
df1 = pd.read_excel("test1.xlsx","Sheet1")
df1 = df1.rename(columns={df1.columns[0]: "time" })
df1 = df1.rename(columns={df1.columns[1]: "1" })
df2 = pd.read_excel("test2.xlsx","Sheet1")
df2 = df2.rename(columns={df2.columns[1]: "2" })
df3 = pd.read_excel("test3.xlsx","Sheet1")
df3 = df3.rename(columns={df3.columns[1]: "3" })
df4 = pd.read_excel("test4.xlsx","Sheet1")
df4 = df4.rename(columns={df4.columns[1]: "4" })
df= pd.concat([df1, df2, df3, df4],axis=1)
df = df.loc[:,~df.columns.duplicated()]

#All Raw Data-----------------------------------------------------------------
ax = df.plot(figsize=(8,6), kind="line", x='time', y='1', color="blue",
                        label="S8 + KCI")
df.plot(kind="line", x='time', y='2', color="red",
                       label="S8 + KCI + FR2", ax=ax)
df.plot(kind="line",x='time', y='3', color="green",
                        label="S8 + DI + FR2", ax=ax)
df.plot(kind="line",x='time', y='4', color="black",
                        label="DI + CI", ax=ax)

ax.set_xscale('log')
ax.set_xlabel("T2 Relaxation Time (ms)")
ax.set_ylabel("Incremental Volume (ml)")
ax.set_title("Preserved Utica Shale")
ax.set_ylim(0,0.02)
ax.set_xlim(0.01,1000)
#Save figures-----------------------------------------------------------------
fig1 = ax.get_figure()
fig1.savefig('Figure1.png',
        bbox_inches='tight', dpi = 1000)
```

Appendix C

PYTHON codes to plot XRF elements distribution.

```
import pandas as pd
df1 = pd.read_csv("environment.csv")
df1 = df1.rename(columns={df1.columns[1]: "environment" })
df2 = pd.read_csv("04.csv")
df2 = df2.rename(columns={df2.columns[1]: "S7+KCI+FR1" })
df3 = pd.read_csv("05.csv")
df3 = df3.rename(columns={df3.columns[1]: "S7+KCI+FR2" })
df= pd.concat([df1, df2, df3],axis=1)
df = df.loc[:,~df.columns.duplicated()]
df["S7+KCI+FR1-Subst"] = df["S7+KCI+FR1"] - df["environment"]
df["S7+KCI+FR2-Subst"] = df["S7+KCI+FR2"] - df["environment"]
#All Raw Data-----------------------------------------------------------------
ax = df.plot(figsize=(8,6), kind="scatter", x='Channel#', y='environment',
color="blue",
                        label="environment")
df.plot(kind="scatter", x='Channel#', y='S7+KCI+FR1', color="red" ,
                        label="S7+KCI+FR1", ax=ax)
df.plot(kind="scatter",x='Channel#', y='S7+KCI+FR2', color="green" ,
                        label="S7+KCI+FR2", ax=ax)
ax.set_xlabel("Channel")
ax.set_ylabel("Intensity")
ax.set_title("Intensity vs Channel - All Raw Data")
ax.set_ylim(0,80000)
ax.set_xlim(0,750)
#Substracted Data-------------------------------------------------------------
ax2 = df.plot(figsize=(8,6), kind="scatter", x='Channel#', y='S7+KCI+FR1-
Subst', color="red",
                        label="S7+KCI+FR1")
df.plot(kind="scatter", x='Channel#', y='S7+KCI+FR2-Subst', color="green"
,
                        label="S7+KCI+FR2", ax=ax2)
ax2.set_xlabel("Channel")
ax2.set_ylabel("Intensity")
ax2.set_title("Intensity vs Channel - Cleaned Data")
ax2.set_ylim(0,80000)
ax2.set_xlim(0,750)
#Save figures
fig1 = ax.get_figure()
fig2 = ax2.get_figure()
fig1.savefig('Figure1.png',
        bbox_inches='tight', dpi = 1000)
fig2.savefig('Figure2.png',
        bbox_inches='tight', dpi = 1000)
```

.

Appendix D

PYTHON codes to plot Embedment results (bar charts).

```
import numpy as np
import matplotlib.pyplot as plt
# data to plot
n_groups = 4
#means_S7_DI_FR1 = (4.89, 17.42, 4.03, 26.34)
#means_S7_DI_FR2 = (5.15, 11.14, 13.73, 30.01)
#means_S7_DI_KCI_FR1 = (1.92, 13.67, 7.91, 23.50)
#means_S7_DI_KCI_FR2 = (3.21, 15.45, 3.03, 21.68)
#means_S7_DI_KCI_CI = (2.35, 11.52, 5.66, 19.53)
#means_1S7_DI = (3.82, 8.42, 12.26, 24.50)
means_CI_DI = (4.03, 8.14, 14.65, 26.82)
means_CI_TAP = (4.17, 12.02, 18.66, 34.85)
# create plot
fig, ax = plt.subplots()
index = np.arange(n_groups)
bar_width = 0.1
opacity = 0.8
rects1 = plt.bar(index, means_CI_DI, bar_width,
alpha=opacity,
color='r',
label='Test-1')
rects2 = plt.bar(index + bar_width, means_CI_TAP, bar_width,
alpha=opacity,
color='g',
label='Test-2')
#plt.xlabel('Minerals')
plt.ylabel('Deformation (%)')
plt.title('Preserved Utica')
plt.xticks(index + bar_width, ('ELASTIC', 'PLASTIC', 'CREEP', 'TOTAL'))
plt.legend()
plt.tight_layout()
plt.show()
#Save figures
fig1 = ax.get_figure()
     fig1.savefig('Figure1.png',
        bbox_inches='tight', dpi = 1000)
```

Appendix E

Walsh, (1981) derive an expression for conductance.

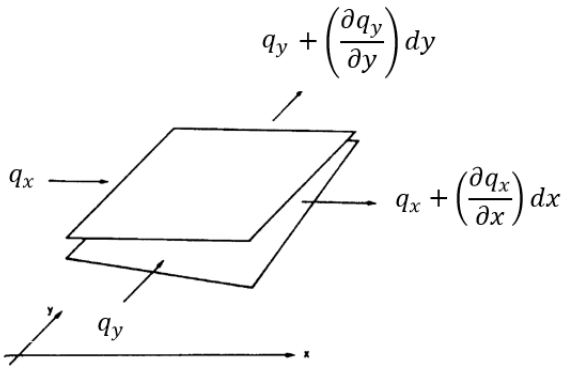

Figure 33. Flow is 2D in the x-y plane (From Walsh, 1981)

$$q_x = \left(\frac{2a^3}{3\mu}\right)\left(\frac{\partial p}{\partial x}\right) \tag{E.1}$$

For incompressible fluid and rock, we get equation (E.2) and (E.3).

$$\frac{\partial q_x}{\partial x} + \frac{\partial q_y}{\partial y} = 0 \tag{E.2}$$

$$\frac{\partial}{\partial x}\left(a^3 * \frac{\partial p}{\partial x}\right) + \frac{\partial}{\partial y}\left(a^3 * \frac{\partial p}{\partial y}\right) = 0 \tag{E.3}$$

Since $\frac{\partial a}{\partial x}$ and $\frac{\partial a}{\partial y}$ are small, then we get equation (E.4).

$$\nabla^2 p = 0 \tag{E.4}$$

Effective conductance from Carslaw et al. 1959

$$\frac{< c > - c}{< c >} = -2\alpha \frac{c - c_i}{c + c_i - \alpha(c - c_i)} \tag{E.5}$$

Since we are concerned with the effects of contact with irregularities on flow, c_i is zero.

$$< k >= \frac{1-\alpha}{1+\alpha} k \tag{E.6}$$

$$k = q \Big/ (\partial p / \partial x) \tag{E.7}$$

From Equation E.1

$$k = 2a^3 \Big/ 3\mu \tag{E.8}$$

Introducing (E.8) into (E.6)

$$< k >= \frac{1-\alpha}{1+\alpha} \left\{ 2a^3 \Big/ 3\mu \right\} \tag{E.9}$$

Where "μ" is viscosity, "a" is half aperture of the fracture, and "α" is the ratio between asperity contact and total surface area of the fracture.

Appendix F

Relative Mineral Content Calculation steps.

The molecular weight of kaolinite $Al_2Si_2O_5(OH)_4 = 27 \cdot 2 + 28 \cdot 2 + 16 \cdot 9 + 4 \cdot 1 = 258$ g/mole

Aluminum fraction in kaolinite = $\frac{27 \cdot 2}{258} = 0.209$

Silicon fraction in kaolinite = $\frac{28 \cdot 2}{258} = 0.217$

Molecular weight of Illite $K_{0.65}Al_2[Al_{0.65}Si_{3.35}O_{10}](OH)_2 = 39 \cdot 0.65 + 27 \cdot 2.65 + 28 \cdot 3.35 + 16 \cdot 12 + 2 \cdot 1 = 384.7$ g/mole

The aluminum fraction in illite = $\frac{27 \cdot 2.65}{384.7} = 0.186$

Silicon fraction in kaolinite = $\frac{28 \cdot 3.35}{384.7} = 0.2438$

Relative concentrations of the elements such as [Al], [Si], [Ca], and [Mg] were taken from the S1calprocess software. Mineral contents are calculated with the following equations.

$$Kaolinite = \frac{[Al]}{2 \cdot 0.209}$$

$$Illite = \frac{[Al]}{2 \cdot 0.186}$$

$$Carbonate = \frac{Ca - \frac{[Mg]}{[24/40]}}{[40/100]}$$

$$Quartz\ (SiO_2) = \left[\frac{[Si] - Kaolinite \cdot 0.217 - Illite \cdot 0.2438}{28}\right] \cdot [28 + 16 \cdot 2]$$

$$Clay = Kaolinite + Illite$$

$$Clay + Carbonate + Quartz = 100\ \%$$

Table 4. Mineralogy of tested preserved Utica Shale Samples

Sample No	XRF, Mineralogy		
	Clay	Quartz	Carbonate
1	53.44	21.81	27.37
2	50.02	18.94	35.54
3	48.99	21.38	34.50
4	54.46	22.18	20.51
5	49.04	21.94	30.33
6	38.10	24.95	36.51
7	39.80	21.33	41.80
8	42.59	23.24	36.34
9	56.18	21.65	19.31
9	44.10	22.99	37.05
10	56.46	20.26	20.43
10	42.65	24.45	36.48
11	56.18	21.65	19.31
11	46.10	22.14	34.29
12	44.03	20.15	38.51
13	42.81	24.26	36.46
14	40.38	24.49	37.06
14	51.99	23.69	21.47
15	49.03	19.66	35.62
15	62.64	20.99	23.53
16	56.12	23.67	17.36
17	46.73	21.48	34.97
18	42.01	20.35	40.80
19	40.71	21.88	39.64
20	37.81	24.03	40.00
21	52.32	22.37	22.46
22	38.89	21.17	43.12

Appendix G

The microscope camera takes images during the displacement-controlled test.

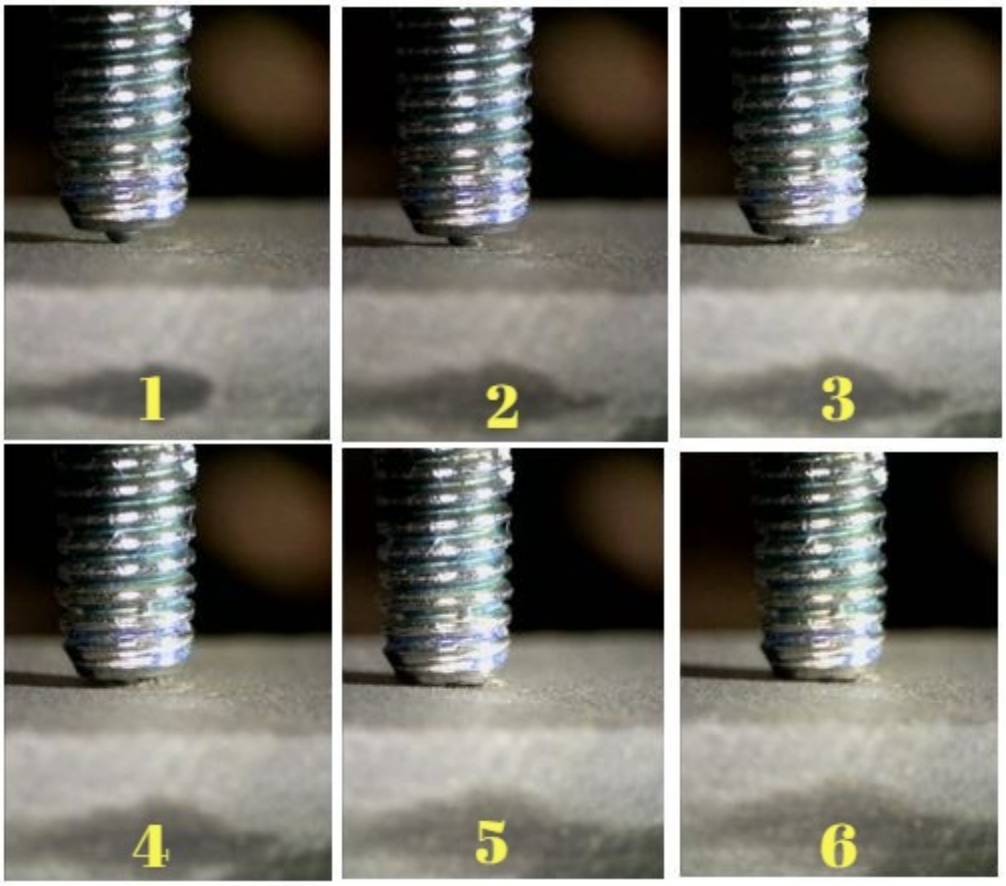

Figure 34. Matrix testing of DI water and surfactants with low clay content shale.

References

Alagoz, E., Wang, H., Russell, R. T., & Sharma, M. M. (2020, September 18). New Experimental Methods to Study Proppant Embedment in Shales. American Rock Mechanics Association.

Alehossein, H. and Hood, M. (1996). State of the art review of rock models for disk roller cutters. Rock Mechanics Tools and Techniques. 2nd North American Rock Mechanics Symposium, Balkema, Rotterdam. pp. 693-700.

Allen, T. D. and Roberts, A. P. (1978). Surfactants for Well Treatments. In Production Operations, Chap. 2, 115–16 Tulsa, Oklahoma: Oil and Gas Consultants Intl. Inc.

Alramahi, B. and MI. Sundberg. (2012). Proppant embedment and conductivity of hydraulic fractures in shales, ARMA Paper#12-291, 46th US Rock Mechanics/Geomechanics Symposium held in Chicago, IL, USA, 24-27 June.

Anderson, H., Bratrud, T., and Delorey, J. (1982). A Logical Approach to Fracture Fluid Selection. *Journal of Canadian Petroleum Technology*, *21*(6).

Andrews, J.S. and Kjorholt, H. (1998). Rock Mechanical Principles Help to Predict Proppant Flowback from Hydraulic Fracture. Paper SPE 47382 presented at the SPE/ISRM Eurorock, Trondheim, Norway, July 8-10.

API RP 42. (1977). Recommended Practices for Laboratory Testing of Surface-Active Agents for Well Stimulation, second edition. Dallas: API.

API RP 61. (1989). Recommended Practices for Evaluating Short Term Conductivity. Washington, DC: API.

Argawal, R. G., Carter, R. D., and Pollock, C.B. (March 1979). "Evaluation of Performance of Low Permeability Gas Wells Stimulated by Massive Hydraulic Fracturing," JPT, pp. 362-372; Trans. AIME; 267.

Barree, R., Cox, S., and Barree, V. (2003). "Realistic Assessment of Proppant Pack Conductivity for Material Selection," Denver, Colorado.

Bauer, K. A. and Bezemer, C. (1967). Prevention of Carbonate Scale Deposition: A Well-Packing Technique with Controlled Solubility Phosphates. *J Pet Technol* **21** (4): 505–514. SPE-2176-PA.

Bates, T. G., Graver, R. M., and Yuster, S. T. (1946). Influence of Clay Content on Water Conductivity of Oil Sands. *Oil Weekly* (October 21): 48.

Blauch, M., Weaver, J., Parker, M., and Todd, B. (1999). New Insights into Proppant-Pack Damage Due to Infiltration of Formation Fines, Paper SPE 56833-MS. SPE Annual Technical Conference and Exhibition, Houston, Texas, Oct. 3-6.

Brannon, H. D. and Ault, M. G. (1991). New, Delayed Borate-Crosslinked Fluid Provides Improved Fracture Conductivity in High-Temperature Applications. Presented at the Annual Technical Conference and Exhibition, Dallas, 6–9 October. SPE-22838-MS.

Carslaw H.S. and Jaeger, J.C. (1959). Conduction of Heat in Solids, 510 pp, Oxford Univ. Press, London.

Cawiezel, K. E., Singh, A. K., Carman, P. S. (2010). The Selection and Optimization of a Surfactant Package to Maximize Cleanup of a High-Density Fracturing Fluid. Presented at

the SPE Deepwater Drilling and Completions Conference, Galveston, Texas, USA, 5–6 October. SPE-136812-MS.

Clark, H. B., Pike, M. T., and Rengel, G. L. (1982). Water-Soluble Fluorochemical Surfactant Well Stimulation Additives. *J Pet Technol* **34** (7): 1565–1569. SPE-9008-PA.

Clark, P. E. and Guler, N. (1983). Prop Transport in Vertical Fractures: Settling Velocity Correlations. Presented at the SPE/DOE Low Permeability Gas Reservoirs Symposium, Denver, 13–16 March. SPE-11636-MS.

Clark, P. E., Harkin, M. W., and Wahl, H. A. (1977). Design of a Large Vertical Prop Transport Model. Presented at the SPE Annual Fall Technical Conference and Exhibition, Denver, 9–12 October. SPE-6814-MS.

Cooke Jr. CE (1973). "Conductivity of Fracture Proppants in Multiple Layers," *Journal of Petroleum Technology,* vol. 25, no. 09, pp. 1101-1107.

Corapcioglu, H., J.L. Miskimins, M. Prasad. (2014). Fracturing Fluid Effects on Young's Modulus and Embedment in the Niobrara Formation. Paper SPE-170835-MS presented at the SPE Annual Technical Conference and Exhibition held in Amsterdam, The Netherlands, 27-29 October.

Coulter, A. W. Jr., Frick, E. K., and Samuelson, M. L. (1983). Effect of Fracturing Fluid pH on Formation Permeability. Presented at the SPE Annual Technical Conference and Exhibition, San Francisco, 5–8 September. SPE-12150-MS.

Coulter, G.R. (1972). The Advantages of High Proppant in Fracture Stimulation, Paper SPE 3298, JPT 1972, Vol.24, No. 6, pp. 643-650.

Daneshy, A. A. (1978). Hydraulic Fracture Propagation in Layered Formations. *SPE J.* **18** (1): 3341. SPE-6088-PA. https://doi.org/10.2118/6088-PA.

Economides, M.J. and Nolte, K.G. (1989). Reservoir Stimulation. Second edition. Houston.

Featherston, A. B., Mihram, R. G., and Waters, A. B. (1959). Minimization of Scale Deposits in Oil Wells by Placement of Phosphates in Producing Zones. *J Pet Technol* **11** (3): 29–32. SPE-1128-G.

Fitzgibbon, J. J. (1984). Sintered Spherical Pellets Containing Clay as a Major Component Useful for Gas and Oil Well Proppants. US Patent No. 4,427,068.

Ford, T. F. (1960). Viscosity Concentration and Fluidity-Concentration Relationships for Suspensions of Spherical Particles in Newtonian Liquids. *J. Phys. Chem.* **64** (9): 1168–1174.

Funkhouser, G. P., Holtsclaw, J., and Blevins, J. J. (2010). Hydraulic Fracturing Under Extreme HPHT Conditions: Successful Application of a New Synthetic Fluid in South Texas Gas Wells. SPE-132173-MS.

Gatlin, C. and Nemir, C. E. (1961). Some Effects of Size Distribution on Particle Bridging in Lost Circulation and Filtration Tests. *J Pet Technol* **13** (6): 575–578. SPE-1652-G-PA.

Gdanski, R. D., Harris, P. C., Lord, D. L. (1991). Analysis of Fann Model 50 for Fracturing Fluid Rheology. Presented at the SPE Production Operations Symposium, Oklahoma City, Oklahoma, USA 7–9 April. SPE-21647-MS.

Gidley, J. L., Holditch, S. A., Nierode, D. E. (1989). *Recent Advances in Hydraulic Fracturing.* Richardson, Texas: Society of Petroleum Engineers.

Graham, J. W., Monaghan, P. H., and Osoba, J. S. (1959). Influence of Propping Sand Wettability on Productivity of Hydraulically Fractured Oil Wells. In *Transactions of the Society Petroleum Engineers,* Vol. 216, SPE-1254-G, 324–329. Richardson, Texas: Society of Petroleum Engineers.

Graham, J. W., Muecke, T. W., and Cooke, C. E. Jr. (1975). Method for Treating Subterranean Formations. US Patent No. 3,929,191.

Greff, K., Greenbauer, S., Huebinger K., and Goldfaden, B. (2014). "The Long-Term Economic Value of Curable Resin-Coated Proppant Tail-in to Prevent Flowback and Reduce Workover Cost," Denver.

Groundwater Protection Council. (2012). FracFocus well records: January 1, 2011, through February 27, 2012: accessed on-line at http://www.fracfocus.org.

Guo, J., Y. Liu. (2012). Modeling of Proppant Embedment: Elastic Deformation and Creep Deformation. SPE-157449.

Gupta, D. V. S. (2009). Unconventional Fracturing Fluids for Tight Gas Reservoirs. Presented at the SPE Hydraulic Fracturing Technology Conference, The Woodlands, Texas, USA, 19–21 January. SPE-119424-MS.

Hall, C. D. Jr. and Dollarhide, F. E. (1964). Effects of Fracturing Fluid Velocity on Fluid-Loss Agent Performance. *J Pet Technol* **16** (5): 555–557. SPE-736-PA.

Hall, C. D. Jr. and Dollarhide, F. E. (1968). Performance of Fracturing Fluid Loss Agents Under Dynamic Conditions. *J Pet Technol* **20** (7): 763–769. SPE-1904-PA.

Hannah, R. R. and Harrington, L. J. (1981). Measurement of Dynamic Proppant Fall Rates in Fracturing Gels Using a Concentric Cylinder Tester. *J Pet Technol* **33** (5): 909–913. SPE-7571-PA.

Harris, P. C., Walters, H. G., and Bryant, J. (2009). Prediction of Proppant Transport From Rheological Data. *SPE Prod & Oper* **24** (4): 550–555. SPE-115298-PA.

Harris, P. C. (1985). Dynamic Fluid Loss Characteristics of Nitrogen Foam Fracturing Fluids. *J Pet Technol* **37** (10): 1847–1852. SPE-11065-PA.

Harris, P. C. (1987). Dynamic Fluid-Loss Characteristics of CO2-Foam Fracturing Fluids. *SPE Prod Eng* **2** (2): 89–94. SPE-13180-PA.

Harris, P. C. (1996). Rheology of Crosslinked Foams. *SPE Prod & Fac* **11** (2): 113–116. SPE-28512-PA.

Hawsey, J. D. and Jacocks, C. L. (1961). The Use of Fluid-Loss Additives in Hydraulic Fracturing of Oil and Gas Wells. Presented at the SPE California Regional Meeting, Bakersfield, California, USA, 2–3 November. SPE-244-MS.

Hawsey, J. D., Whitesell, L. B., and Kepley, N. A. (1964). Injection of a Bactericide-Surfactant During Hydraulic Fracturing - A New Method of Corrosion Control. SPE-978-MS.

Herbert, E.G., Pharr, G.M., Oliver, W.C., Lucas, B.N., Hay, J.L. (2001). On the measurement of stress-strain curves by spherical indentation, Thin Solid Films, 398–399: 331-335.

Hertz, H. (1863). Miscellaneous Papers, ed. Jones and Schott, London.

Hewitt, C. H. (1963). Analytical Techniques for Recognizing Water-Sensitive Reservoir Rocks. *J Pet Technol* **15** (8): 813–818. SPE-594- PA.

Howard, G. C. and Fast, C. R. (1970). *Hydraulic Fracturing.* Richardson, Texas: Monograph Series, Society of Petroleum Engineers.

Hower, W. F. (1974). Influence of Clays on the Production of Hydrocarbons. SPE-4785-MS.

Huang, J., R. Safari, O. Perez, E.F. Fragachan. (2019). Reservoir Depletion-Induced Proppant Embedment and Dynamic Fracture Closure. SPE 195135-MS.

Jennings, A. R. Jr. (1996). Fracturing Fluids - Then and Now. *J Pet Technol* **48** (7): 604–610. SPE-36166-JPT.

Jones, F. O. Jr. (1964). Influence of Chemical Composition of Water on Clay Blocking of Permeability. *J Pet Technol* **16** (4): 441–446. SPE-631-PA.

Johnson, C. K. and Armbruster, D. R. (1982). Particles Covered with a Cured Infusible Thermoset Film and Process for Their Production.US Patent No. 4,439,489.

King, G. E. (1977). Factors Affecting Dynamic Fluid Leak off With Foam Fracturing Fluids. SPE-6817-MS.

Knox, J. A., Waters, A. B., and Arnold, B. B. (1962). Checking Paraffin Deposition by Crystal Growth Inhibition. SPE-443-MS.

Kou, S., Lindquist, P.A., and Tan, X. (1995). An analytical and experimental investigation of rock indentation fracture. *Proceedings of the 8th International Congress on Rock Mechanics*, Tokyo. International Society for Rock Mechanics, Lisbon. pp. 181-184.

Kutter, H. and Sanio, H.P. (1982). Comparative study of performance of new and worn disc cutters on a full-face tunneling machine. *Proceedings of Tunneling '82*. Institution of Mining and Metallurgy, London. pp. 127-133.

Lacy, L.L., A.R. Rickards, and D.M. Biden. (1998). Fracture aperture and Embedment Testing in Soft Reservoir Sandstone. SPE Drilling & Completion, 13(1): 25-29.

Lacy, L.L., A.R. Rickards, and A.A. Syed. (1997). Embedment and Fracture Conductivity in Soft Formations Associated with HEC, Borate, and Water-based Fracture Designs. SPE-38590-MS.

Lawn, BR and Wilshaw, R. (1975). Indentation fracture: principles and applications. *Journal of Materials Science*, 10, 1049-1081.

Lawrence, S. C., Kalenchuk, A. C., Ranicar, K. (2009). Volatile Phosphorus Free Gellants for Hydrocarbon-Based Fracturing Systems. *SPE Prod & Oper* **24** (4): 556–561. SPE-115481-MS.

Leopoldo, S. (2010). New High-Density Fracturing Fluid to Stimulate a High Pressure & High-Temperature Tight Gas Sandstone Producer Formation in Saudi Arabia. SPE-130236-MS.

Li, L., Eliseeva, K., Eliseev, V. (2009). Well Treatment Fluids Prepared with Oilfield Produced Water. **S**PE-124212-MS.

Liang, F., Sayed, M., Al-Muntasheri, G., and Chang, F.F. (2015). "Overview of Existing Proppant Technologies and Challenges," Manama, Bahrain, 8-11 March.

Maslowski M, Kasza P, Wilk K. (2018). Studies on the effect of the proppant embedment phenomenon on the effective packed fracture in shale rock. Acta Geodyn. Geomater., 15, No.2 (190), 105-115,2018.

Mayerhofer, M., Lolon, E., Warpinski, N., Cipolla, C., Walser, D., and Rightmire, C. (2008, November). What is stimulated rock volume?. *SPE Paper 119890 in SPE Shale Gas Production Conference*.

McCall, J. M. Jr. and Johnson, R. L. (1984). Paraffin Treatment in the Well Service Industry. *Proc,* Southwestern Petroleum Short Course, Lubbock, Texas, April, 457–468.

McDaniel, R. R., Deysarkar, A. K., Callanan, M. J. (1985). An Improved Method for Measuring Fluid Loss at Simulated Fracture Conditions. *SPE J.* **25** (4): 482–490. SPE-10259-PA.

McGowen, J. M., Vitthal, S., Parker, M. A. (1993). Fluid Selection for Fracturing High-Permeability Formations. SPE-26559-MS.

Meyer, E. (1908). Untersuchungen u¨ber Ha¨rteprufung und Ha¨rte. Z. Ver. Deutsche Ing. 52, 645–654.

Milton-Taylor, D., Stephenson, C., and Asgian, M.I. (1992). Factors Affecting the Stability of Proppant in Propped Fractures: Results of a Laboratory Study. SPE 24821-MS.

Mirakyan, A., Abad, C., Parris, M. (2009). Rheological Characterization of Novel Delayed-Transition Metal Crosslinked Fracturing Fluids: Correlation with First Field Applications. SPE-121757-MS.

Miskimins J. L. (2019). *Hydraulic Fracturing Fundamentals and Advancements.* Richardson, Texas: Monograph Series, Society of Petroleum Engineers.

Monaghan, P. H., Salathiel, R. A., Morgan, B. E. (1959). Laboratory Studies of Formation Damage in Sands Containing Clays. SPE-1162-G.

Much, MG and Penny, G.S. (1987). Long-term Performance of Proppants under Stimulated Reservoir Conditions. SPE 14615-MS.

Mungan, N. (1965). Permeability Reduction Through Changes in pH and Salinity. *J Pet Technol* **17** (12): 1449–1453. SPE-1283-PA.

Nelson, P.P., Ingraffea, AR, and O'Rourke, T.D. (1985). TBM performance prediction using rock fracture parameters. *International Journal of Rock Mechanics and Mining Sciences & Geomechanics Abstracts*, 22 (3), 189-192.

Nolte, K. G. and Plahn, S. V. (1993). An Assessment of the Effect of Fracturing-Fluid Performance on Well Productivity. SPE-26601-MS.

Novotny, E. J. (1977). Proppant Transport. Presented at the SPE Annual Technical Conference and Exhibition, Denver, 9–12. October. SPE-6813-MS.

Palisch, T. and Saldungaray, P.M. (2013). "Understanding Ceramic Proppants: Are They All Created Equal?" Oman.

Palmer, I. D., Fryar, R. T., Tumino, K. A. (1991). Comparison Between Gel-Fracture and Water-Fracture Stimulations. SPE-23415-MS.

Peard, N. S., Macaluso, M. L., Griffin, M. C., Andress, R., & Callanan, M. J. (1991, January 1). Improved Fracturing Techniques Increase Productivity in the AWP (Olmos) Field. Society of Petroleum Engineers.

Penny, G. S., Conway, M. W., and Briscoe, J. E. (1983). Enhanced Load Water-Recovery Technique Improves Stimulation Results. SPE-12149-MS.

Penny, G. S. (1987). Evaluation of the Effects of Environmental Conditions and Fracturing Fluids Upon the Long–Term Conductivity of Proppants. SPE-16900-MS.

Peters, F. W. and Stout, C. M. (1977). Clay Stabilization During Fracturing Treatments with Hydrolysable Zirconium Salts. *J Pet Technol* **29** (2): 187–194. SPE-5687-PA.

Pharr, G.M., W.C. Oliver, F.R. Brotzen. (1991). On the generality of the relationship among contact stiffness, contact area, and elastic modulus during indentation.

Powell, R. J., Terracina, J. M., McCabe, M. A. (1999). Shallow Gas Development: Stimulation Fluids. *J Can Pet Technol* **38** (8). PETSOC-99-08-02.

PropTester Inc. and Kelrik LLC. 2019. Proppant Market Report. March.

Pye, D. S. and Smith, W. A. (1973). Fluid Loss Additive Seriously Reduces Fracture Proppant Conductivity and Formation Permeability. Presented at the Fall Meeting of the Society of Petroleum Engineers of AIME, Las Vegas, 1–3 October. SPE-4680-MS.

Reed, M. G. (1972). Stabilization of Formation Clays with Hydroxy-Aluminum Solutions. *J Pet Technol* **24** (7): 860–864. SPE-3694-PA.

Reinicke, A., B. Legarth, G. Zimmermann, E. Huenges, and G. Dresenn. (2006). Hydraulic fracturing and formation damage in a sedimentary geothermal reservoir. ENGINE–Enhanced Geothermal Innovative Network for Europe Workshop 3, stimulation of reservoir and microseismicity, Kartause Ittingen, Zürich, 29, VI – 1.VII, Switzerland.

Reinicke, A., E. Rybacki, S. Stanchits, E. Huenges, and G. Dresenn. (2010). Hydraulic fracturing stimulation techniques and formation damage mechanisms – Implications from laboratory

testing of tight sandstone – proppant systems. Chemie der Erde - Geochemistry, 70, 107–117.

Roodhart, L., Kuiper, T.O., and Davies, D.R. (1986). Proppant Rock Impairment during Hydraulic Fracturing. SPE-15629.

Samuel, M. M., Card, R. J., Nelson, E. B. (1999). Polymer-Free Fluid for Fracturing Applications. *SPE Drill & Compl* **14** (4): 240–246. SPE-59478-PA.

Sato, K., and M. Ichikawa. (1998). Post-Frac analysis indicating multiple fractures created in a volcanic formation. SPE 39513-MS.

Settari, A. (1985). A New General Model of Fluid Loss in Hydraulic Fracturing. *SPE J.* **25** (4): 491–501. SPE-11625-PA.

Sloat, B. (1963). Controlled Solubility Phosphates - New Application Techniques Simplify Scale Prevention in Waterfloods and Producing Wells. SPE-760-MS.

Smith, C. F., Pavlich, J. P., and Solvinsky, R. L. (1964). Potassium, Calcium Treatments Inhibit Clay Swelling. *Oil and Gas Journal* (November 30): 80.

Sneddon, I.N. (1965). Int. J. Eng. Sci. 3-47.

Shah, S. N. (1982). Proppant Settling Correlations for Non-Newtonian Fluids Under Static and Dynamic Conditions. *SPE J.* **22** (2): 164–170. SPE-9330-PA.

Shah, S. N., Asadi, M., and Lord, D. L. (2001). Proppant Transport Characterization of Hydraulic-Fracturing Fluids Using a High-Pressure Simulator Integrated with a Fiber-Optic/Light-Emitting-Diode (LED) Vision System. *SPE Prod & Fac* **16** (1): 42–49. SPE-69210-PA.

Shumaker, E. F., Raines, V. B., and Warenbourg, P. A. (1978). LeakOff Control Techniques Improve Efficiency of Acid Fracturing Treatments. SPE-7168-MS.

Stewart, J. B. and Coulter, A. W. (1959). Increased Fracturing Efficiency by Fluid Loss Control. *Pet. Eng.* (June): B–43.

Stiff, H. A. Jr. and Davis, L. E. (1952). A Method for Predicting the Tendency of Oil Field Waters to Deposit Calcium Sulfate. *J Pet Technol* **4** (2). SPE-130-G.

Tabor, D. (1951). Hardness of Metals. Clarendon Press. Oxford.

Tan, X.C., Kou, S.Q., and Lindquist, P.A. (1996). Simulation of rock fragmentation by indenters using DDM and fracture mechanics. Rock Mechanics Tools and Techniques: Proceedings of the 2nd North American Rock Mechanics Symposium, Balkema, Rotterdam. pp. 685-692.

Tannich, J. D. (1975). Liquid Removal from Hydraulically Fractured Gas Wells. *J Pet Technol* **27** (11): 1309–1317. SPE-5113-PA.

Terracina, J.M., J.M. Turner, D.H. Collins, and S.E. Spillars. (2010). Proppant selection and its effect on the results of fracturing treatments performed in shale formations. SPE 135502.

Tinsley, J. M. (1967). Design Techniques for Chemical Fracture-Squeeze Treatments. *J Pet Technol* **19** (11): 1493–1499. SPE-1771-PA.

Volk, LJ, J.R. Clarence, B.C. Herbert, and S.S. Judy. (1981). Embedment of High Strength Proppant into Low-Permeability Reservoir Rock. SPE/DOE 9867.

Vlis, A.C., Haafkens, R., Schipper, B.A., and Visser, W. (1975). Criteria for Proppant Placement and Fracture Conductivity. SPE-5367.

Walsh, J.B. (1981). Effect of pore pressure and confining pressure on fracture permeability, Int. J. of Rock Mech. Min. Sci. & Geomech. Abstr., 18, 429-435.

Wang, Y., and Miskimins, J. (2010, November). Experimental Investigations of Hydraulic Fracture Growth Complexity in Slickwater Fracturing Treatments. SPE Paper-137515.

Waters, G. A., Lewis, R. E., & Bentley, D. (2011, January 1). The Effect of Mechanical Properties Anisotropy in the Generation of Hydraulic Fractures in Organic Shales. Society of Petroleum Engineers.

Weaver, J., Blauch, M., Parker, M., and Todd, B. (1999). Investigation of Proppant-Pack Formation Interface and Relationship to Particulate Invasion, SPE-54771-MS.

Wheaton, W. E., Lipari, S. A., Morris, M. D. (1991). A Case Study of High-Temperature Wells Fractured Using Multiple Fluids to Improve Conductivity and Well Performance. SPE-21033-MS.

Wijk, G. (1989). The stamp test for rock drillability classification. International Journal of Rock Mechanics and Mining Sciences & Geomechanics Abstracts, 26 (1), 37-44.

Wilcox, C., Fuss, T., Shi, J., Thompson, M., and Herskovits, R. (2015). Proppant Selection Criteria and Their Influence on Performance of North Dakota Oil-Rich Shale Wells. URTEC-2154615-MS.

Zigrye, J. L., Whitfill, D. L., and Sievert, J. A. (1985). Fluid-Loss Control Differences of Crosslinked and Linear Fracturing Fluids. *J Pet Technol* **37** (2): 315–320. SPE-12153-PA.

Vita

Ekrem Alagoz was born in Adiyaman, Turkey. After finishing his high school education, he joined the Petroleum and Natural Gas Engineering Department at Iskenderun Technical University, Hatay, Turkey, in 2011. He graduated from the same department with a bachelor's degree in 2015. He first started working as a temporary English Teacher at the Ministry of Education for about four months. Later, he started his first master's education in Petroleum and Natural Gas Engineering Department at Istanbul Technical University in 2016 while he was working as a part-time physic teacher in Istanbul. He then started working in the geothermal service company as a drilling engineer for one year with the master's education simultaneously. In 2018, he got the scholarship by The Republic of Turkey for graduate studies in the United States; then, he started The Hildebrand Department of Petroleum and Geosystems Engineering program at The University of Texas at Austin in 2019 January. Upon the completion of his master's degree, he will go back to Turkey and work for the General Directorate of Mineral Research and Exploration (MTA) as a petroleum engineer.

Permanent email address: ekremalagoz93@gmail.com

This thesis was typed by the author.